Geotextiles and Geomembranes 50 (2022) 20–39

Contents lists available at ScienceDirect

Geotextiles and Geomembranes

journal homepage: www.elsevier.com/locate/geotexmem

Interface pullout resistance of polymeric strips embedded in marginal tropical soils

R.C. Pierozan [a,*], G.L.S. Araujo [b], E.M. Palmeira [b], C. Romanel [a], J.G. Zornberg [c]

[a] Department of Civil & Environmental Engineering, Pontifical Catholic University of Rio de Janeiro, Rio de Janeiro, RJ, Brazil
[b] Department of Civil & Environmental Engineering, University of Brasilia, Brasilia, DF, Brazil
[c] Department of Civil, Architectural & Environmental Engineering, The University of Texas at Austin, Austin, TX, USA

ARTICLE INFO

Keywords:
Reinforced soil
Pullout resistance
Interface shear resistance
Polymeric strips
Tropical soils

ABSTRACT

This paper presents an experimental and analytical evaluation of factors affecting the interface pullout resistance of polymeric strips embedded in marginal soils, with a particular interest in supporting the partial replacement of natural sands by intensely weathered tropical soils in reinforced soil structures, which have often been considered marginal fills in design guidelines. Large-scale pullout tests were conducted to evaluate the soil-geosynthetic interface pullout resistance, which also provided quantitative insight into the local increases in vertical stresses acting on the reinforcements due to pullout. Based on the experiments, analytical models were developed and calibrated to establish the relationship between confinement and soil-geosynthetic interface pullout resistance. The relationship between actual and initial stresses could then be represented in terms of a linear model in which the angular coefficient corresponds to the ratio between the apparent and actual friction coefficients (f^*/f). This analytical relationship was found to represent a useful design tool since it directly correlates with soil geotechnical properties. The use of lateritic soils to partially replace coarse-grained soils in reinforced soil structures was found to be feasible for mixtures involving up to 25% of lateritic soils, with higher fractions affecting the interface resistance significantly.

1. Introduction

Reinforced soil walls are structures with linear reinforcement inclusions aiming at providing additional resistance in the form of tensile stresses that develop under working stress conditions (e.g. Schlosser and Bastick, 1991). The internal stability of these structures depends on the frictional resistance that develops on the soil-reinforcement interface as well as the bearing resistance provided by the transverse elements of certain types of reinforcement. Coarse-grained soils, such as clean sands and gravels, can lead to enhanced frictional and dilatant contributions to strength (e.g. Schlosser and Bastick, 1991; Alfaro et al., 1995; Loli et al., 2018), which may not fully develop on the interface between reinforcements and fine-grained soils (e.g. Dai et al., 2015; Zhang et al., 2020).

Theoretical (e.g. Palmeira, 2004; Abdelouhab et al., 2010; Cardile et al., 2017), and numerical (e.g. Abdelouhab et al., 2011; Wang et al., 2016; Noorzad and Badakhshan, 2017) methods have been used to simulate the mechanism of interface pullout resistance that develops under field conditions. Pullout tests provide insight into the responses of reinforcements embedded in reinforced soil structures (Palmeira, 2009), facilitating the quantification of the pullout resistance between fill soils and different reinforcement types, including geogrids (e.g. Palmeira, 1987; Teixeira et al., 2007; Sieira et al., 2009; Moraci and Cardile, 2009; Abdi and Arjomand, 2011; Ezzein and Bathurst, 2014; Bathurst and Ezzein, 2016; Wang et al., 2016; Abdi and Mirzaeifar, 2017; Kayadelen et al., 2018), fibers (e.g. Zornberg, 2002; Yang et al., 2003; Tang et al., 2016), cellular confinement systems (e.g. Khedkar and Mandal, 2009), steel meshes (e.g. Lajevardi et al., 2013; Suksiripattanapong et al., 2013), and polymeric strips (e.g. Abdelouhab et al., 2010, 2011; Razzazan et al., 2018, 2019; Cui et al., 2019; Zhang et al., 2020).

The scarcity of adequate fill soils nearby construction sites may lead to considerable additional costs. Moreover, awareness of the negative sustainability impact related to the extraction of natural sands and gravels has been growing in recent years, prompting researchers to take notice and search for alternative construction materials. The use of non-standard soils as fills in retaining structures has been reported to involve soil-rock mixtures (e.g. Yang et al., 2014), copper slag (e.g. Prasad and

* Corresponding author.
E-mail addresses: rodrigopierozan@esp.puc-rio.br (R.C. Pierozan), gregorio@unb.br (G.L.S. Araujo), palmeira@unb.br (E.M. Palmeira), romanel@puc-rio.br (C. Romanel), zornberg@mail.utexas.edu (J.G. Zornberg).

https://doi.org/10.1016/j.geotexmem.2021.08.004
Received 14 May 2021; Received in revised form 15 July 2021; Accepted 25 August 2021
Available online 2 September 2021
0266-1144/© 2021 Elsevier Ltd. All rights reserved.

Notation

α	Scale effect correction factor (dimensionless)
β	Slope inclination (degrees)
γ_{nat}	Unit weight of soil in its natural state (kN/m^3)
$\Delta\sigma_v$	Local stress increase (kPa)
$\Delta\sigma_{v,max}$	Local stress increase under peak conditions (kPa)
δ_{face}	Face displacement (m)
$\delta_{face,max}$	Face displacement under peak conditions (m)
δ_h	Horizontal displacement (m)
δ_v	Vertical displacement (m)
$\sigma_{v,0}$	Initial vertical stress (kPa)
σ_v	Vertical stress (kPa)
$\sigma_{v,max}$	Vertical stress under peak conditions (kPa)
τ	Shear stress (kPa)
τ_{max}	Shear stress under peak conditions (kPa)
ϕ_s	Soil friction angle (degrees)
$\phi_{s,sec}$	Secant soil friction angle (degrees)
ϕ_{sg}	Soil-geosynthetic interface friction angle (degrees)
$\phi_{sg,sec}$	Secant soil-geosynthetic interface friction angle (degrees)
ψ	Angle of dilation (degrees)
b_e	Distance between external boundaries of the strips (m)
b_i	Distance between internal boundaries of the strips (m)
b_s	Width of a single strip (m)
c	Coefficient used in Eq. (15) (dimensionless)
C	Correction factor indicated in Eq. (16) (dimensionless)
C_0, C_1, χ	Coefficients used in Eq. (16) (dimensionless)
c_s	Cohesion intercept of the soil shear resistance (kPa)
C_c	Coefficient of curvature (dimensionless)
C_u	Coefficient of uniformity (dimensionless)
D_{max}	Maximum diameter of diamond mesh as in Fig. 4(a) (m)
D_{min}	Minimum diameter of diamond mesh as in Fig. 4(a) (m)
f	Actual friction coefficient (dimensionless)
f_b	Pullout interaction coefficient (dimensionless)
f^*	Apparent friction coefficient (dimensionless)
f_0	The maximum value for f^* (dimensionless)
f_1	The minimum value for f^* (dimensionless)
F_c	Fines content (mass fraction with a diameter smaller than 0.075 mm) (%)
g_1, g_2	Coefficients used in Eq. (1) (dimensionless)
G_s	Specific gravity (dimensionless)
h_1, h_2	Coefficients used in Eq. (2) (dimensionless)
j_1, j_2	Coefficients used in Eq. (3) (dimensionless)
$k_{20°C}$	Hydraulic conductivity at 20 °C (m/s)
l_1, l_2	Coefficients used in Eq. (7) (dimensionless)
L_g	Geosynthetic embedment (m)
n_1, n_2	Coefficients used in Eq. (8) (dimensionless)
P	Pullout resistance (kN)
p_a	Atmospheric pressure (kPa)
PI	Plasticity index (%)
P_{max}	Pullout resistance under peak conditions (kN)
r_1, r_2	Coefficients used in Eq. (13) (dimensionless)
R^2	Coefficient of determination (%)
s_1, s_2	Coefficients used in Eq. (14) (dimensionless)
W_g	Geosynthetic width considering a pair of strips (m)
w_L	Liquid limit (%)
w_{opt}	Optimum water content (%)
w_P	Plastic limit (%)
x_i	Relative position at the reference axis in Fig. 8 and Fig. 9 (m)
z	Depth of installation (m)
z_0	Break-point depth (m)

Ramana, 2016; Zhang et al., 2018), construction and demolition recycled aggregates (e.g. Santos et al., 2014; Vieira et al., 2016; Gálvez-Martos et al., 2018), and fine-grained soils (e.g. Zornberg and Mitchell, 1994; Mitchell and Zornberg, 1995; Abdi and Arjomand, 2011; Portelinha et al., 2013; Sukmak et al., 2015; Abd and Utili, 2017; Chen et al., 2018).

The use of intensely weathered tropical soils, also known as lateritic soils, as fills in reinforced soil structures may offer economic, technical, and environmental benefits due to their wide availability in tropical and sub-tropical climate zones (e.g. Araujo et al., 2009, 2021), such as sizeable regions of South America, Asia, and Oceania. However, tropical soils often exhibit a distinct geotechnical behavior, relative to their counterpart soils found in temperate zones (e.g. Gidigasu, 1972), which has frequently hindered the use of the design guidelines available for such materials. Intensely weathered soils are characterized by micro-structural bonding resulting from an accumulation of hydrated iron and aluminum oxides (sesquioxides), forming soil aggregations larger than individual clay particles, which can ultimately lead to enhanced mechanical behavior relative to typical cohesive soils found in temperate zones (Mahalinga-Iyer and Williams, 1994; Ng et al., 2019; Araujo et al., 2021). These characteristics favor support the use of lateritic soils as construction material in several geotechnical structures, such as roadway bases and sub-bases (e.g. Rezende et al., 2005), and reinforced soil structures (e.g. Sukmak et al., 2016) under predefined conditions.

The use of polymeric strips instead of metallic strips can be particularly advantageous when dealing with marginal fills, such as intensely weathered soils, to avoid degradation of these elements over time due to corrosion. Only limited information is currently available in the technical literature regarding the pullout resistance of polymeric strips embedded in lateritic soils. A comprehensive understanding of the possibility of partially or entirely replacing granular fills with intensely weathered soils could provide more practical ranges of applications of these materials in reinforced soil structures.

This paper provides insight into the interface pullout resistance of polymeric strips embedded in marginal tropical soils, with particular emphasis on the evaluation of factors influencing soil-geosynthetic pullout and interface shear resistance as well as a discussion of their relevance from a design perspective. The geomechanical properties of the soils and the results from pullout tests were used as input in analytical methods used to predict pullout responses, providing tools deemed relevant to the design of reinforced soil structures.

2. Fill soils

The experimental component of this research was developed at the University of Brasilia (Federal District, Brazil) (Pierozan, 2018). Samples of the following soils were collected from natural deposits in the central region of Brazil: (1) a clean uniform sand, extracted from a fluvial deposit at Rio das Almas (State of Goias, Brazil); and (2) a weathered fine-grained soil, collected at the Experimental Field of the University of Brasília Geotechnical Engineering Graduate Program (Federal District, Brazil).

2.1. Geotechnical characterization

Fill soils were prepared following ASTM D421-85 (2007). Particles with dimensions smaller than 0.075 mm (fines content, F_c) were removed from the natural sand, and particles larger than two (2) millimeters were removed from both the natural sand and clayey soil to avoid their influence on test results. Following these procedures, mixtures were created with the clean uniform sand and the fine-grained soil

(lateritic weathered soil) at different weight fractions.

The nomenclature used for the different samples in this paper consists of an acronym (S for sand, and L for lateritic soil) followed by the weight fraction of the mixture's components, which yielded the following sample designations: S100-L0 for 100% clean uniform sand; S75-L25 for a mixture containing 75% clean uniform sand and 25% marginal tropical soil; S50-L50 for a mixture containing 50% clean uniform sand and 50% marginal tropical soil; and S0-L100 for 100% marginal tropical soil.

The X-Ray Diffraction (XRD) technique was utilized to evaluate the mineralogical composition of the clean uniform sand (S100-L0) and fine-grained soil (S0-L100) using a Rigaku Ultima IV apparatus, while the chemical composition of these soils was determined via the X-Ray Fluorescence (XRF) spectrometry technique.

According to mineralogical composition tests, the clean uniform sand consisted primarily of quartz (82.3%), while muscovite (12.6%), kaolinite (3.4%), and rutile (1.7%) were also detected as secondary minerals. The mineralogical composition of the clean uniform sand was consistent with that of natural silica sands (e.g. Klein and Hurlbut, 1993), which are a well-accepted fill in reinforced soil structures. The intensely weathered soil consisted of gibbsite (35.3%) and quartz (35.3%), while secondary minerals included kaolinite (16.2%), hematite (6.8%), rutile (4.0%), and anatase (2.4%), which are characteristic of the lateritic soils found in the Federal District of Brazil (e.g. Rezende et al., 2005; Araujo et al., 2009, 2021).

Chemical composition tests indicated that the clean uniform sand was primarily composed of silica (SiO_2 – 81.2%), while secondary components included aluminum oxide (Al_2O_3 - 6.1%), iron oxide (Fe_2O_3 – 4.9%), titanium dioxide (TiO_2 – 2.7%), and potassium oxide (K_2O – 1.9%), with 1.5% additional components and 1.7% loss on ignition. The main components of the intensely weathered soil (S0-L100) were aluminum oxide (Al_2O_3 - 38.8%), silica (SiO_2 – 23%), and iron oxide (Fe_2O_3 – 15.7%), while secondary components included titanium dioxide (TiO_2 – 2.1%) and 0.3% other components, with 20.1% loss on ignition. The intensely weathered soil was classified as a lateritic soil according to the tropical residual soil classification (e.g. Catt, 1990).

Laboratory tests were also utilized to establish the specific gravity of solids (ASTM D854-14, 2014), Atterberg limits (ASTM D4318-17e1, 2017), and particle size distribution analyses (ASTM D422-63e2, 2007, and ASTM D4221-18, 2018). To determine the dimensions of individual soil particles, grain size tests were conducted via conventional testing procedures using a Dispersing Agent (D.A.) following ASTM D422-63e2 (2007). The double hydrometer test (ASTM D4221-18, 2018) was also carried out for the samples containing lateritic soil (S75-L25, S50-L50, and S0-L100) used in this study, which includes an alternative procedure employing neither chemical dispersants (D.A.) nor solution stirring. It should be noted that the mechanical behavior of intensely weathered soils is largely affected by the dimensions of water-stable soil aggregations instead of individual particles (e.g. Mahalinga-Iyer and Williams, 1994; Ng et al., 2019, Araujo et al., 2021), supporting this alternate testing procedure (hydrometer test with and without D.A.) to evaluate the possibility of formation of soil aggregations.

Minimum and maximum void ratios were determined for the clean uniform sand (S100-L0) following the specifications provided by ASTM D4253 (2016) and ASTM D4254-16 (2016), respectively, while Standard Proctor compaction tests (ASTM D698-12, 2021) were carried out for the samples containing lateritic soil (S75-L25, S50-L50, and S0-L100).

Constant head (ASTM D2434-19, 2019) and falling head (ASTM D5084-16a, 2016) hydraulic conductivity tests were conducted on saturated compacted samples of the clean uniform sand (S100-L0), and samples containing lateritic soil (S75-L25, S50-L50, and S0-L100), respectively. The fill requirements suggested by the Federal Highway Administration (Berg et al., 2009) served as a reference for specimen preparation: (*i*) a relative density of 95% when considering the clean uniform sand (S100-L0); and (*ii*) a relative compaction corresponding to 95% of the maximum dry unit weight (Standard Proctor test), and tolerance of $\pm 2\% \times w_{opt}$ for the water content, with w_{opt} referring to the optimum value, when considering samples containing lateritic soil (S75-L25, S50-L50, and S0-L100).

A summary of the geotechnical characterization is presented in Table 1 and particle size distribution curves are given in Fig. 1.

The behavior of the compacted samples was considerably affected by the fine-grained particles added to the sand-lateritic soil mixtures. The minimum and maximum void ratios of the clean uniform sand (S100-L0) were equal to 0.58 and 0.83, respectively. The voids between sand grains were observed to progressively fill with cohesive particles for mixtures M75-L25 and M50-L50, in relation to the clean uniform sand (S100-L0). Proctor compaction tests indicated an optimum water content of 12%, 16%, and 22%, respectively, for samples S75-L25, S50-L50, and S0-L100, respectively, while the maximum dry unit weights associated with these soils were 18.2 kN/m^3, 17.8 kN/m^3, and 15.7 kN/m^3, respectively.

The arrangement of soil grains into aggregations had a considerable effect on size-distribution characteristics and associated fines content (the mass fraction with a diameter smaller than 0.075 mm, as indicated in Table 1). Hence, even though the lateritic soil (S0-L100) was classified as silty sand (SM) according to the USCS when considering tests with no dispersing agent (ASTM D4221-18, 2018), the overall geotechnical behavior presented by this material was more consistent with low plasticity silts (ML) considering the use of a dispersing agent (ASTM D422-63e2, 2007). Mixtures with lateritic soil content greater than 25% by weight (S75-L25, and M50-L50) presented plastic behavior due to the contribution of fine-grained particles.

Based on the particle size distribution curves (Fig. 1), the percentage dispersion of the lateritic weathered soil (S0-L100) was determined as 25%, indicating this material has low susceptibility to erosion. This behavior agrees with the findings of previous works, which have highlighted the satisfactory geotechnical behavior of sample S0-L100 as pavement base and sub-base in roadway projects (e.g. Rezende et al., 2005) and also benefitted from the low compressibility presented by this material after compaction. Samples S75–25 and S50-L50 presented 70% and 50% dispersion, respectively, indicating these materials are more susceptible to erosion than the tropical soil (S0-L100) used in this research. Permeability coefficients at 20 °C ($k_{20°C}$) of 3×10^{-4} m/s, 1×10^{-7} m/s, 7×10^{-9} m/s, and 4×10^{-9} m/s were measured for samples S100-L0, S75-L25, S50-L50, and S0-L100, respectively. Consequently, adequate surface water management and drainage must be implemented when using sand-lateritic soil mixtures.

Table 1
Geotechnical properties of fill materials and considering tests with and without Dispersing Agent (D.A.).

Properties		Fill Materials			
		S100-L0	S75-L25	S50-L50	S0-L100
G_s		2.64	2.65	2.66	2.67
Atterberg Limits	w_P (%)	–	20	23	28
	w_L (%)	–	21	27	39
	PI (%)	–	1	4	11
With D.A.	C_c	1.0	28.0	~100	~200
	C_u	2.4	~60	~300	~1000
	F_c (%)	0	16.2	31.9	64.8
	USCS	SP	SM	SM	ML
Without D.A.	C_c	1.0	2.6	6.8	~20
	C_u	2.4	7.1	33.0	~80
	F_c (%)	0	10.1	17.8	31.4
	USCS	SP	SW	SM	SM

Note: The symbols and abbreviations indicated in Table 1 are: specific gravity (G_s); plastic limit (w_P); liquid limit (w_L); plasticity index (PI); coefficient of curvature (C_c); coefficient of uniformity (C_u); fines content (the mass fraction with a diameter smaller than 0.075 mm, F_c); and the Unified Soil Classification System (USCS, as in ASTM D4287-17e1, 2017).

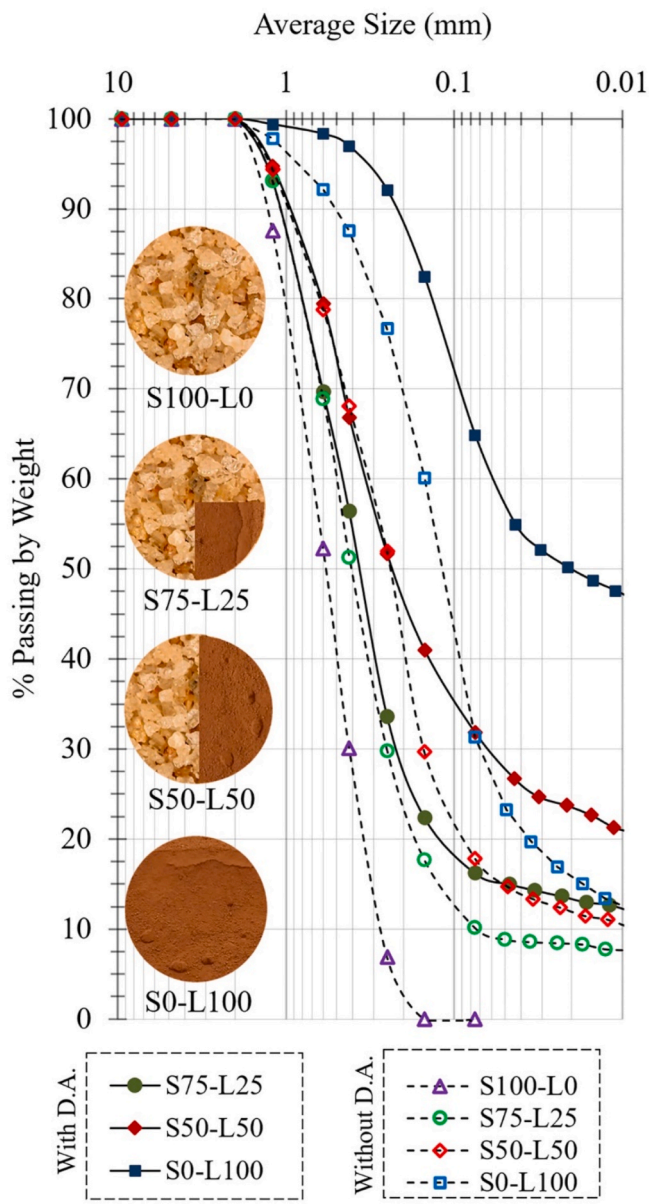

Fig. 1. Particle size distribution curves with and without Dispersing Agent (D. A.), and schematic representation of tested samples.

2.2. Soil internal shear resistance

As-compacted specimens (unsaturated) with a cross-section measuring 100 mm × 100 mm and a height of 20 mm were subjected to direct shear tests aiming at determining shear resistance mechanisms. The following compaction requirements were adopted in this research: (*i*) a relative density of 95% when considering the clean uniform sand (S100-L0), and a water content of approximately 0.25%; and (*ii*) a relative compaction corresponding to 95% of the maximum dry unit weight (Standard Proctor test), and tolerance of $\pm 2\% \times w_{opt}$ for the water content, before and after testing, with w_{opt} referring to the optimum value, when considering samples containing lateritic soil (S75-L25, S50-L50, and S0-L100).

The weight of soils in their natural state (γ_{nat}), as expressed in this paper, corresponded to as-compacted samples (unsaturated), i.e. considering a relative density of 95% for sample S100-L0, and a relative compaction of 95% for samples S75-L25, S50-L50, and S0-L100. Accordingly, the values assumed by γ_{nat} corresponded to 14.16 kN/m^3, 19.41 kN/m^3, 19.56 kN/m^3, and 18.19 kN/m^3 for samples S100-L0, S75-L25, S50-L50, and S0-L100, respectively, while the dry unit weights associated with these samples corresponded to 14.12 kN/m^3, 17.33 kN/m^3, 16.86 kN/m^3, and 14.91 kN/m^3, respectively.

These specimens were subjected to direct shear tests to define soil internal friction angles and cohesive intercepts under unsaturated conditions, following ASTM D3080/D3080M-11 (2011). These tests were completed under a constant shear displacement rate of 0.05 mm/min, which was selected to avoid excess pore water pressures during shearing (ASTM D3080/D3080M-11, 2011). A representation of soil internal shear resistance parameters is shown in Fig. 2, with shear stresses relative to horizontal shear displacements shown in Fig. 2(a), and vertical shear displacements relative to horizontal shear displacements indicated in Fig. 2(b).

The Mohr-Coulomb envelopes corresponding to the internal friction (ϕ_s) and interface friction (ϕ_{sg}) considering the maximum shear stresses are presented in Fig. 2(c). It can be observed that the internal shear strength of the clean uniform sand (S100-L0) involved primarily a frictional resistance component, while the mixtures (S75-L25 and S50-L50) and lateritic soil (S0-L100) presented an additional contribution the cohesion component of resistance. The internal friction angles (ϕ_s) were equal to 44°, 40°, 38°, and 33° for samples S100-L0, S75-L25, S50-L50, and S0-L100, respectively, considering the maximum shear stresses.

According to Fig. 2(c), the cohesion intercepts of samples S75-L25, S50-L50, and S0-L100 assumed values of 11 kPa, 21 kPa, and 30 kPa, respectively. As expected, the relatively large percentage of sesquioxides [aluminum oxide (38.8%) and iron oxide (15.7%)] relative to silica (23%) characteristic of the lateritic soil (S0-L100) caused the formation of water-stable micro-aggregations consistent with previous works (e.g. Mahalinga-Iyer and Williams, 1994; Ng et al., 2019). The particle arrangement of the mixtures (S75-L25, and S50-L50) also benefitted from the bonding provided by the accumulation of sesquioxides on the surface of the sand particles, which inhibited the frictional dilatant behavior that would be expected from sandy soils, as is discussed subsequently in this paper.

The secant soil friction angles ($\phi_{s,sec}$) are presented in Fig. 2(d). An analytical model was used to represent the soil secant friction angles in terms of initial stress conditions ($\sigma_{v,0}$) given the values assumed by the coefficients of determination (R^2 larger than 90%) when contrasting predicted values with experimental data, which is valid in the range of 12.5 kPa $\leq \sigma_{v,0} \leq$ 200 kPa. The following equations were found to fit the experimental results well:

$$\phi_{s,sec} = e^{g_1 + g_2 \times \ln\left(\frac{\sigma_{v,0}}{p_a}\right)} \tag{1}$$

where g_1 and g_2 are dimensionless coefficients associated with $\phi_{s,sec}$; and p_a is the atmospheric pressure (101 kPa).

The coefficients associated with the fitting equations discussed in this paper are summarized in Table 2, including those related to Eq. (1). It is worth noting that the proposed equations and coefficients are valid for the materials studied in the current research, and additional research may be required for extrapolation for other materials and testing conditions. The main objective of these fitting equations is to assess the trend of the evaluated parameters, as discussed later in this paper.

2.3. Angles of dilation

Previous studies (e.g. Schanz and Vermeer, 1996) have indicated that plane strain and axisymmetric testing conditions can lead to a similar angle of dilation, although the soil friction angle may be affected considerably by the testing configuration. Accordingly, a conventional direct shear apparatus was adapted to better quantify the angle of dilation (Jewell, 1989; Simoni and Houlsby, 2006). The adaptation of the direct shear device consisted of attaching the piston at which the normal efforts are applied to the upper frame, thus ensuring a uniform distribution of vertical displacements on top of the specimen, as shown

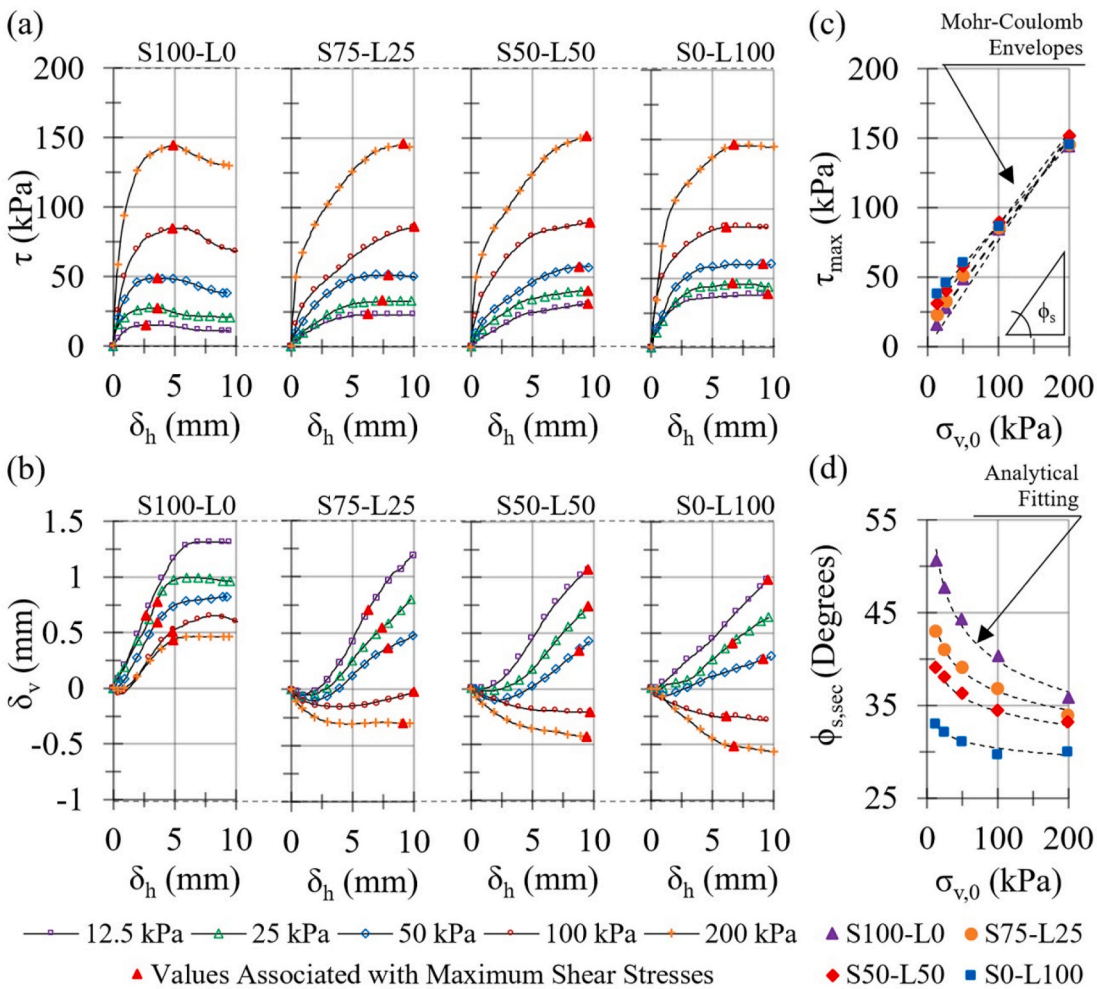

Fig. 2. Soil shear resistance after conventional direct shear tests: (a) Shear stresses relative to horizontal shear displacements (δ_h); (b) Vertical shear displacements (δ_v) relative to horizontal shear displacements; (c) Soil shear resistance envelopes; and (d) Soil secant friction angles.

Table 2
Analytical fitting equations, and associated parameters, for variables associated with the interface shear resistance.

Eq.	Relationship	Coef.	Compacted Soil			
			S100-L0	S75-L25	S50-L50	S0-L100
(1)	$\phi_{s,sec} = function(\sigma_{v,0})$	g_1	3.6860	3.5950	3.5450	3.4080
		g_2	−0.1205	−0.0831	−0.0601	−0.0399
		R^2	98.21%	98.68%	98.98%	90.13%
(2)	$\Psi = function(\sigma_{v,0})$	h_1	1.5930	−0.2113	−1.3960	−4.0000
		h_2	−0.6950	−0.7675	−1.0000	−1.0000
		R^2	100%	98.32%	100%	100%
	$\phi_{sg,sec} = function(\sigma_{v,0})$	j_1	3.4840	3.4970	3.4560	3.4140
(3)		j_2	−0.0955	−0.0650	−0.0313	−0.0372
		R^2	98.65%	97.79%	94.51%	94.70%
(7)	$P_{max} = function(\sigma_{v,0})$	l_1	−0.8019	0.0427	0.1666	0.2000
		l_2	7.4340	4.3400	3.1060	2.0710
		R^2	98.89%	99.68%	98.65%	99.97%
(8)	$P/P_{max} = function\left(\frac{\delta_{face}}{\delta_{face,max}}\right)$	m_1	0.4948	0.7094	0.7919	0.8753
		m_2	0.4266	0.2142	0.1327	0.1033
		R^2	96.74	98.66	98.53	99.46
(9)	$\sigma_v = function(\sigma_{v,0})$	f^*/f	2.0747	1.5051	1.2808	1.1699
		R^2	99.67%	98.95%	99.08%	99.87%

in Fig. 3(a). As-compacted (unsaturated) samples, following the aforementioned compaction requirements, were subject to adapted direct shear testing under a constant shear displacement rate of 0.05 mm/min. Shear stresses relative to horizontal shear displacements are shown in Fig. 3(b).

Vertical shear displacements relative to horizontal shear displacements are presented in Fig. 3(c). The angles of dilation were calculated as the tangent of the quotient between vertical and horizontal displacements immediately before reaching the maximum shear stresses, i.e. the inclination of the δ_v *versus* δ_h curves [Fig. 3(c)]. Mohr-Coulomb

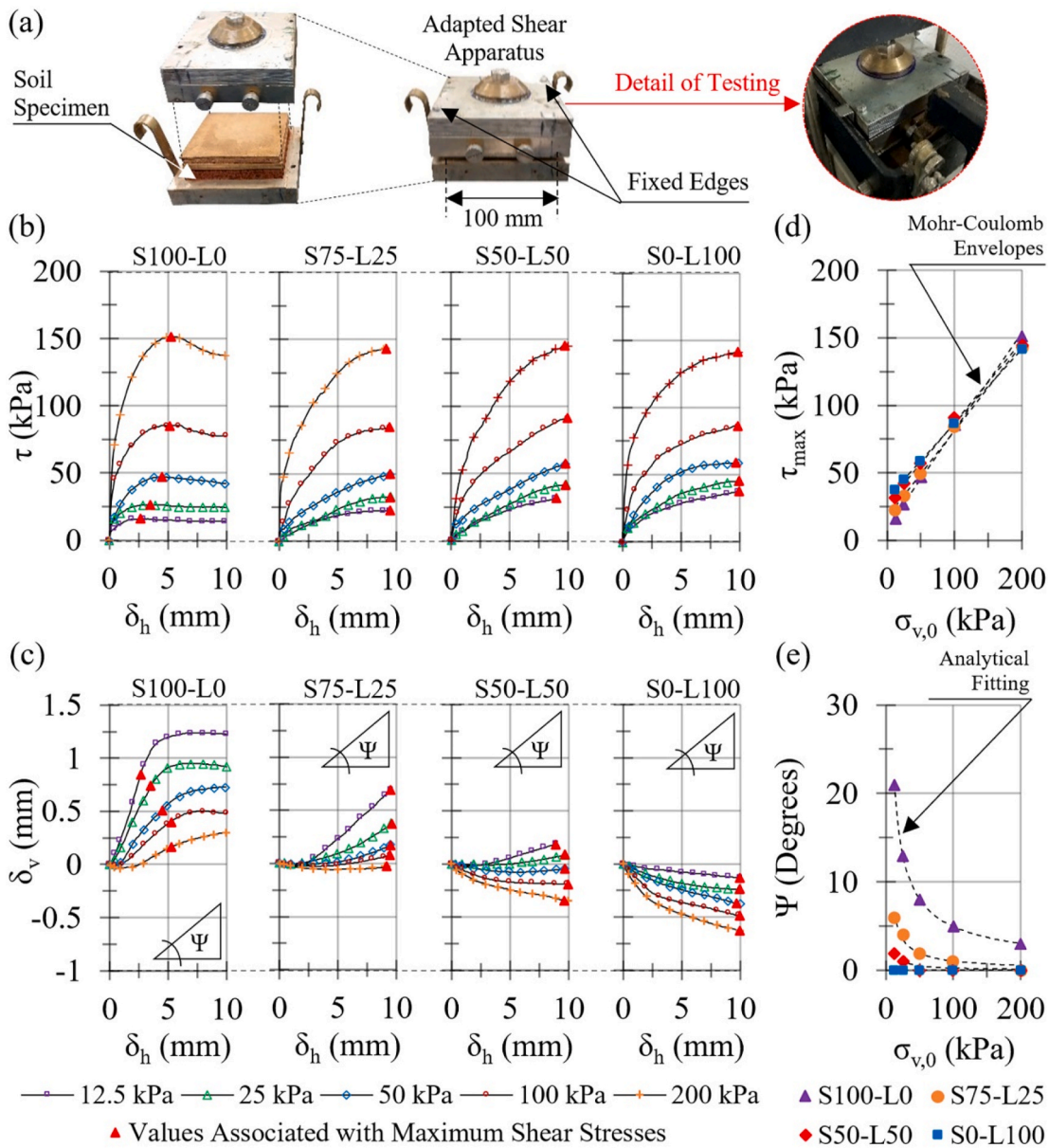

Fig. 3. Adapted direct shear tests conducted to provide insight on the angles of dilation: (a) Shear stresses relative to horizontal shear displacements; (b) Vertical shear displacements relative to horizontal shear displacements; (c) Shear resistance envelopes; and (d) Angles of dilation relative to initial stress conditions.

envelopes are presented in Fig. 3(d), while the angles of dilation (ψ), are presented in Fig. 3(e). Overall, dilatant behavior was observed for the clean uniform sand (S100-L0), while this component of shear strength was not observed from the mixtures (S75-L25 and S50-L50) due to interparticle bonding. The secant friction angles of the clean uniform sand (S100-L0) presented coefficients of determination (R^2) larger than 95% with the values predicted by the relation proposed by Bolton (1986), i.e. $\phi_{s,sec} = \phi_{cv} - 0.8 \times \Psi$, in which the constant volume friction angle (ϕ_{cv}) is equal to 33° for quartz sands. However, this relation was not suitable for the mixtures.

An analytical model was used to represent the angles of dilation in terms of initial stress conditions ($\sigma_{v,0}$) given the values assumed by the coefficients of determination (R^2 larger than 95%) when contrasting predicted values with experimental data, which is valid in the range of 12.5 kPa $\leq \sigma_{v,0} \leq$ 200 kPa. The following equations were found to fit the experimental results well:

$$\psi = e^{h_1 + h_2 \times \ln\left(\frac{\sigma_{v,0}}{p_a}\right)} \tag{2}$$

where h_1 and h_2 are dimensionless coefficients associated with ψ; and p_a is the atmospheric pressure (101 kPa).

3. Soil-geosynthetic interface shear resistance

As compacted (unsaturated) soil specimens with a cross-section measuring 100 mm × 100 mm and a height of 20 mm were molded from compacted blocks under the aforementioned compaction requirements. These specimens were subjected to direct shear tests to define interface friction angles under unsaturated conditions to determine the soil-geosynthetic interface shear properties, following ASTM D5321/D5321M-20 (2020). These tests were completed under a constant shear displacement rate of 0.05 mm/min, which was selected to avoid excess pore water pressures during shearing (ASTM

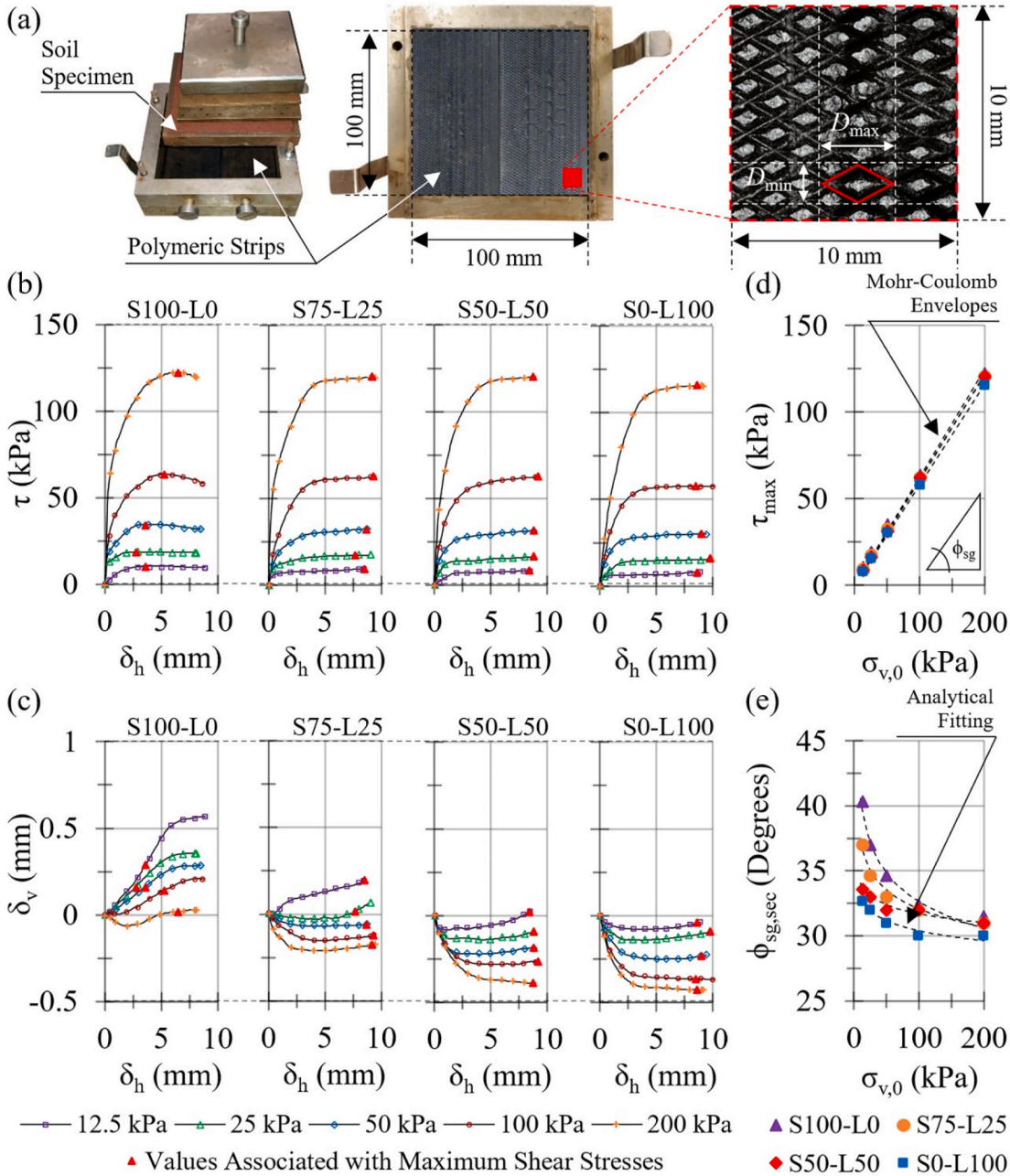

Fig. 4. Interface shear resistance after direct shear tests: (a) Shear stresses relative to horizontal shear displacements; (b) Vertical shear displacements relative to horizontal shear displacements; (c) Interface shear resistance envelopes; and (d) Secant friction angles.

D3080/D3080M-11, 2011).

The polymeric strips used in this investigation involve a polyethylene sheet encasement which aimed at enhancing interface friction relative to smooth reinforcements. Detail of the interface features, including the diamond mesh found on both top and bottom surfaces of the reinforcement, is shown in Fig. 4(a), along with a representation of the direct shear device used for testing. The average dimensions of these diamond-shaped elements were one (1) millimeter high (distance between trough and crest), two (2) millimeters for the smallest diameter (D_{min}), and three (3) millimeters for the largest diameter (D_{max}), according to 3D microscopy tests (LEXT microscope, model OLS4100). The reported tensile strength of each polymeric strip was 50 kN. This comparatively large tensile strength may be attributed to the high tenacity polyester fibers (HTPET) found in the core of the polymeric strips. Since a key focus of this research was the behavior of these elements under working conditions, the tensile properties were characterized at strain levels of 2% and 5%, resulting in elastic moduli of 2.43 GPa and 2.27 GPa, respectively.

The Mohr-Coulomb envelopes corresponding to the interface friction (ϕ_{sg}) associated with maximum shear stresses are presented in Fig. 4(b), while the vertical shear displacements relative to the horizontal shear displacements are shown in Fig. 4(c). The soil-geosynthetic interface friction angles (ϕ_{sg}) were equal to 36°, 35°, 35°, and 33° for samples S100-L0, S75-L25, S50-L50, and S0-L100, respectively, considering the maximum shear stresses. Furthermore, it can be observed that the components of soil friction angles were greater than the interface friction angles, indicating that interface sliding did not mobilize as much resistance as internal shear, which is consistent with the behavior described in previous works (e.g. Elias et al., 2001; Gao et al., 2010). Unlike the internal resistance, adhesion did not play an important role in

interface shear resistance, as evidenced by the Mohr-Coulomb envelopes presented in Fig. 4(d). In this regard, AASHTO (2017) and the French code (NF P94-270, 2009) recommend that the contribution from cohesive components of interface shear strength should not be considered in design procedures.

An analytical model was used to represent the angles of dilation in terms of initial stress conditions ($\sigma_{v,0}$), as shown in Fig. 4(e), given the values assumed by the coefficients of determination (R^2 larger than 95%) when contrasting predicted values with experimental data, which is valid in the range of 12.5 kPa $\leq \sigma_{v,0} \leq$ 200 kPa. The following equation was found to fit the experimental results well:

$$\phi_{sg,sec} = e^{j_1 + j_2 \times \ln\left(\frac{\sigma_{v,0}}{p_a}\right)} \quad (3)$$

where j_1 and j_2 are dimensionless coefficients associated with $\phi_{sg,sec}$; and p_a is the atmospheric pressure (101 kPa).

A summary of direct shear testing results is presented in Table 3. It should be noted that the determination of internal and interface shear resistance parameters, along with the estimates concerning the angles of dilation, were performed using unsaturated specimens with the initial moisture content targeting the optimum values (w_{opt}), along with the preestablished compaction requirements. Unsaturated testing conditions were selected in this research because they were considered more representative of actual working conditions to which retaining walls are subjected, also denoting the anticipated contribution of suction on the shear resistance of cohesive samples (S75-L25, S50-L50, and S0-L100), relative to the clean uniform sand (S100-L0).

4. Soil-geosynthetic interface pullout resistance

A view of the pullout testing equipment used in the experimental component of this study is presented in Fig. 5(a), with an overview of the most relevant components of the device given in Fig. 5(b). The pullout box, designed by Palmeira (1996), has internal dimensions of 1450 mm (length), 890 mm (width), and 570 mm (height). The original box was enhanced with a series of components, including a flexible hydraulic diaphragm-loading device, horizontal and vertical reaction frames, enhanced geosynthetic clamps, pullout actuator, and instrumentation.

The external instrumentation consisted of one (1) load cell and two (2) displacement transducers installed on the face of the box, while the internal instrumentation consisted of five (5) pressure cells installed at the positions denoted as PC-1, PC-2, PC-3, PC-4, and PC-5. The pressure cells were adapted to provide a maximum stress capacity of 100 kPa, being installed on top of the reinforcements at positions PC-1, PC-2, and PC-3, and embedded within the compacted soil at positions PC-4 and PC-5. Also, the pressure cells used in this research had a diameter of 50 mm and a thickness of 6 mm. It is important to highlight that the local stress increase ($\Delta\sigma_v$) is influenced by the distance relative to the reinforcement element (Schlosser and Bastick, 1991). Thus, the pressure cells positioning directly on top of the reinforcements aimed at capturing the local stress increase on the soil-geosynthetic interface. The instrumentation devices were connected to a data acquisition system (LYNX, model ADS0500-16-W).

Polymeric strips can be installed using different configurations. They include a double strap arrangement (e.g. Miyata et al., 2019), in which the reinforcement is installed in closely spaced pairs of straps oriented

Table 3
Summary of the direct shear data testing results, considering maximum shear stress data points.

		Data Points	$\sigma_{v,0}$ (kPa)				
			12.5	25	50	100	200
Soil Internal Shear Resistance	**S100-L0**	δ_h (mm)	2.61	3.56	3.58	4.77	4.88
		δ_v (mm)	0.66	0.78	0.60	0.51	0.43
		τ (kPa)	15.20	27.40	48.70	84.80	144.20
	S75-L25	δ_h (mm)	6.30	7.43	7.93	10.00	9.15
		δ_v (mm)	0.71	0.55	0.37	−0.02	−0.30
		τ (kPa)	22.66	32.73	51.49	85.80	145.30
	S50-L50	δ_h (mm)	9.58	9.56	8.81	9.75	9.44
		δ_v (mm)	1.07	0.74	0.34	−0.21	−0.43
		τ (kPa)	31.12	40.53	57.70	89.70	151.90
	S0-L100	δ_h (mm)	9.45	6.60	9.14	6.09	6.70
		δ_v (mm)	0.98	0.41	0.26	−0.26	−0.52
		τ (kPa)	38.12	45.62	60.04	86.70	145.30
Angles of Dilation	**S100-L0**	δ_h (mm)	2.66	3.54	4.50	5.22	5.29
		δ_v (mm)	0.85	0.75	0.52	0.40	0.17
		τ (kPa)	15.81	26.48	47.04	85.33	151.41
	S75-L25	δ_h (mm)	9.50	9.54	9.50	9.45	9.17
		δ_v (mm)	0.69	0.37	0.17	0.08	−0.03
		τ (kPa)	22.39	32.96	49.71	84.65	143.18
	S50-L50	δ_h (mm)	8.95	9.75	9.72	9.96	9.67
		δ_v (mm)	0.19	0.08	−0.05	−0.19	−0.34
		τ (kPa)	31.40	41.84	57.19	91.42	145.07
	S0-L100	δ_h (mm)	9.92	9.90	9.68	9.88	9.88
		δ_v (mm)	−0.13	−0.24	−0.37	−0.49	−0.63
		τ (kPa)	37.78	45.46	58.84	86.31	141.36
Interface Shear Resistance	**S100-L0**	δ_h (mm)	3.65	2.74	3.59	5.26	6.52
		δ_v (mm)	0.29	0.16	0.16	0.14	0.02
		τ (kPa)	10.60	18.84	34.60	63.50	122.40
	S75-L25	δ_h (mm)	8.47	7.64	8.68	9.29	9.12
		δ_v (mm)	0.19	0.01	−0.06	−0.12	−0.18
		τ (kPa)	9.40	17.30	32.47	62.49	120.17
	S50-L50	δ_h (mm)	8.43	8.80	8.79	9.17	8.70
		δ_v (mm)	0.02	−0.09	−0.19	−0.27	−0.39
		τ (kPa)	8.30	16.24	31.24	62.49	120.00
	S0-L100	δ_h (mm)	8.57	9.75	8.97	8.55	8.64
		δ_v (mm)	−0.05	−0.09	−0.23	−0.37	−0.43
		τ (kPa)	8.00	15.62	30.04	57.74	115.47

Note: The soil samples used for pullout testing, as indicated in Table 3, met the following criteria: water content of approximately 0.25%, the relative density of 95% ± 3% for sample S100-L0; and water content of w_{opt} ± 2%, and relative compaction of 95% ± 3% for samples S75-L25, S50-L50, and S0-L100.

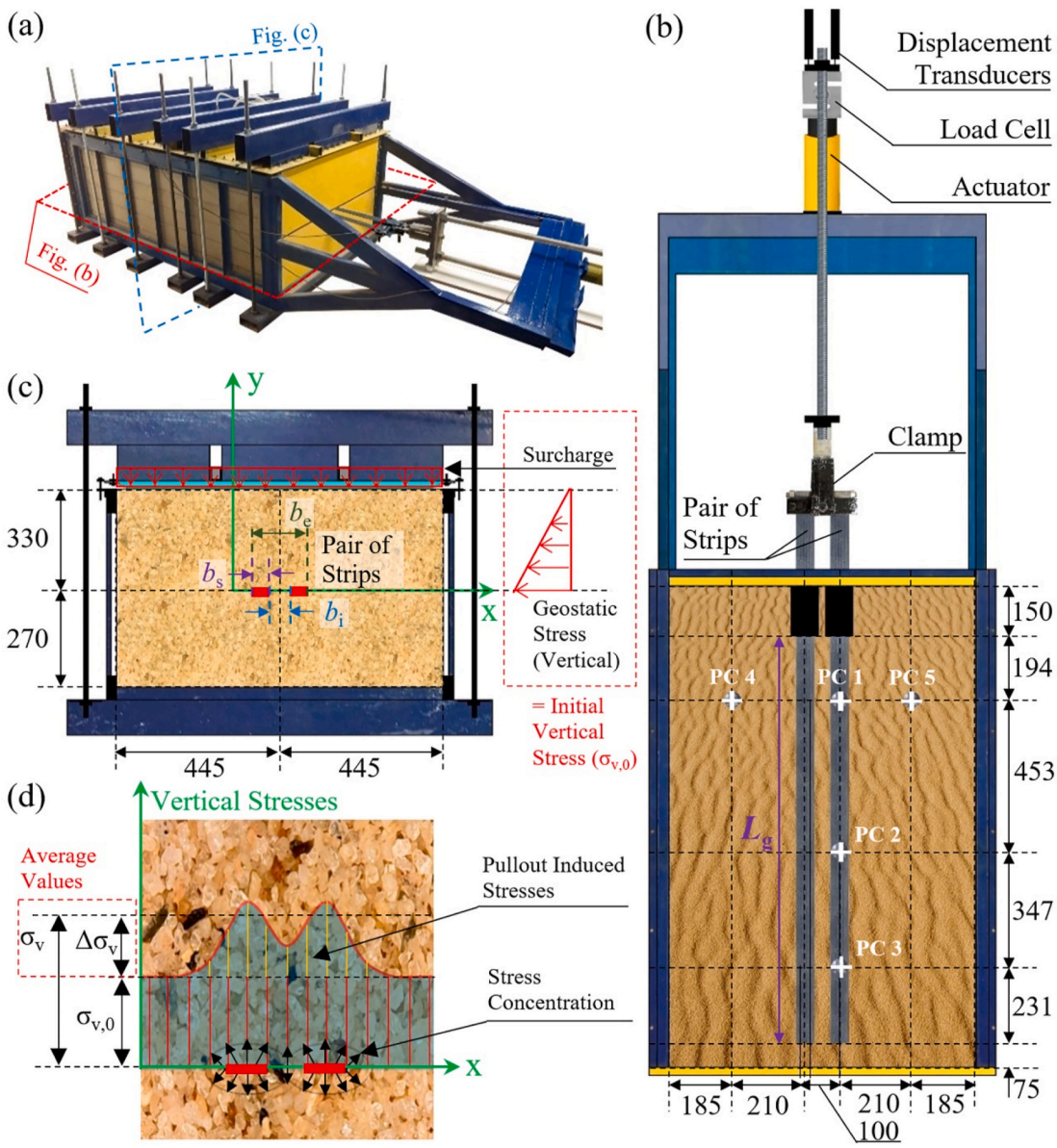

Fig. 5. Pullout apparatus (in millimeters): (a) Equipment overview; (b) Reinforcement installation and instrumentation positioning; (c) Vertical cross-section, and initial stress configuration; and (d) Presumed stress configuration on the reinforcement plane during the pullout of a pair of polymeric strips.

perpendicular to the facing unit, which can facilitate the development of arching (Abdelouhab et al., 2010). Other installation methods include: (*i*) single straps positioned perpendicular to the facing panel (e.g. Abdelouhab et al., 2010; Miyata et al., 2019); (*ii*) straps installed in a splayed pattern, in which the strap material is looped at the connection with the concrete facing (e.g. Luo et al., 2015); and (*iii*) U-shaped far end configurations (e.g. Razzazan et al., 2019). In the present study, the double strap arrangement was used, with the geosynthetic embedment length denoted as L_g, as also represented in Fig. 5(b).

A vertical cross-section of the pullout box is presented in Fig. 5(c), along with an illustration of the initial stress configuration on the reinforcement plane. The width of a single polymeric strip reinforcement is represented by (b_s), and the distances between external and internal boundaries of the strips by (b_e) and (b_i), respectively. The total reinforcement width (W_g) was 100 mm, with b_s and b_i being 50 mm and 150 mm, respectively. The thickness of the polymeric strips was uniform and equal to 4 mm. The initial vertical stress ($\sigma_{v,0}$) acting on the reinforcement plane, as indicated in Fig. 5(c), can be grouped into two major components: (*i*) surcharge stress, which is applied by loading devices on the upper surface of the soil specimen; and (*ii*) vertical geostatic soil pressure on the reinforcement, which depends on the confinement level attributed to the compacted soil. However, the resistance mechanisms developed at the interface between the reinforcement and dense, compact, dilatant fill materials can lead to a local stress increase along with the reinforcements during pullout (e.g. Schlosser and Bastick, 1991; Teixeira et al., 2007, Georgiou et al., 2020; Kido and Kimura, 2021), as indicated in Fig. 5(d). Under failure conditions, the actual vertical stress acting on reinforcements can be expressed as follows (Schlosser and Bastick, 1991):

$$\sigma_{v,max} = \sigma_{v,0} + \Delta\sigma_{v,max} \tag{4}$$

where $\sigma_{v,max}$ is the vertical stress acting on top of the reinforcements under failure conditions, and $\Delta\sigma_{v,max}$ is the local increase in vertical stresses under failure conditions.

The interface shear resistance associated with pullout tests may be determined according to the following equation (Schlosser and Bastick, 1991):

$$\tau_{max} = f \times \sigma_{v,max} = f^* \times \sigma_{v,0} \quad (5)$$

where τ_{max} is the shear resistance under failure conditions, f is the actual friction coefficient, and f^* is the apparent friction coefficient.

Considering the definitions expressed in Eqs. (4) and (5), the friction coefficients can be back-calculated based on pullout test results, as follows (e.g. Elias et al., 2001):

$$P_{max} = 2 \times L_g \times W_g \times f^* \times \sigma_{v,0} = 2 \times L_g \times W_g \times f \times \sigma_{v,max} \quad (6)$$

where P_{max} is the maximum pullout resistance.

4.1. Pullout resistance

The internal surfaces of the pullout box were lined with double layers of lubricant and polyethylene film, aiming at reducing sidewall friction. Sand pluviation (e.g. Lo Presti et al., 1992) and vibration techniques were used to achieve the target density for the clean uniform sand (S100-L0), while samples containing lateritic soil (S75-L25, S50-L50, and S0-L100) were compacted with a mechanical hammer. Sand pluviation and vibration were carried out in layers with a height of 90 mm after compaction, considering the aforementioned compaction requirements. Initial vertical stresses ($\sigma_{v,0}$) of 12.5 kPa, 25 kPa, and 50 kPa at the reinforcements were adopted for testing. Tests were performed under unsaturated conditions. The rate of pullout displacement was 1 mm/min, as recommended by ASTM D6706-01 (2013), and the maximum displacement of the external end of the strip was 100 mm.

A depiction of the pullout test results is given in Fig. 6, with pullout resistance curves shown in Fig. 6(a), and a summary of pullout testing results is presented in Table 4. It can be noted that the frictional and dilatant behavior of the clean uniform sand (S100-L0) provided it with enhanced pullout resistance in relation to samples containing lateritic soil (S75-L25, S50-L50, and S0-L100). It is believed that the interparticle bonding caused by the accumulation of hydrated iron and aluminum oxides (sesquioxides) inhibited the frictional and dilatant behavior of the sandy grain skeleton, agreeing with previous works (e.g. Mahalinga-Iyer and Williams, 1994; Ng et al., 2019) which focused on the internal shear resistance of lateritic soils.

The pullout resistance envelopes are presented in Fig. 6(b). The following observations can be made based on these test results: (*i*) the initial vertical stresses ($\sigma_{v,0}$) affected considerably the pullout resistance; (*ii*) pullout responses were also affected by the different fill types, indicating that the geomechanical properties of fills correlate to a certain degree with the mobilization of interface friction resistance mechanisms; and (*iii*) the maximum pullout forces (P_{max}) were found to be directly proportional to frontal displacements at failure ($\delta_{face,max}$), also depending on the type of fill.

Given the influence of the stress levels observed on the friction resistance mechanisms, an equation was fitted to the failure envelopes (Fig. 6(b)) and is expressed as follows:

$$P_{max} = l_1 + l_2 \times \sqrt{\sigma_{v,0} \times L_g \times W_g} \quad (7)$$

where l_1 and l_2 are dimensionless model coefficients.

The relationship expressed in Eq. (7) had a strong statistical agreement ($R^2 > 95\%$) with the experimental results for each set of data points and is valid in the range of $0 < \sigma_{v,0} \leq 50$ kPa. The values assumed by the dimensionless model coefficients l_1 and l_2 are summarized in Table 2.

In an attempt to focus the analysis on the effect of geomechanical fill properties on pullout behavior, a dimensionless representation of the pre-failure phase of the load-displacements curves ($P < P_{max}$) was also investigated, with P corresponding to the pullout load associated with a given face displacement (δ_{face}). The aforementioned dimensionless curves are depicted in Fig. 7, with Fig. 7(a) indicating the relationship between P/P_{max} and $\delta_{face}/\delta_{face,max}$. The 1:1 reference line in this figure represents a hypothetical soil in which any percentage of the pullout loads (0%–100% of P_{max}) is directly correlated with an equivalent percentage of the face displacements (0%–100% of $\delta_{face,max}$), i.e. a soil that does not benefit from the additional frictional resistance provided by the coarse-grained soil skeleton.

It can be observed that the shape of the dimensionless load-displacement curves was somewhat affected by the type of fill material. For instance, the curves associated with the clean uniform sand (S100-L0) presented a larger curvature concerning the curves associated with the lateritic soil (S0-L100). Conversely, the curves representing different vertical stresses (i.e. 12.5 kPa, 25 kPa, and 50 kPa) for a given type of soil presented less variability amongst each other. Accordingly, the curves associated with different stress conditions did not present significant differences amongst each other considering a confidence level of 95% for a specific type of fill soil, supporting the interpolation of a single analytical curve to represent each material.

The analytical model used to represent the dimensionless load-displacement curves consisted of a hyperbolic function as recom-

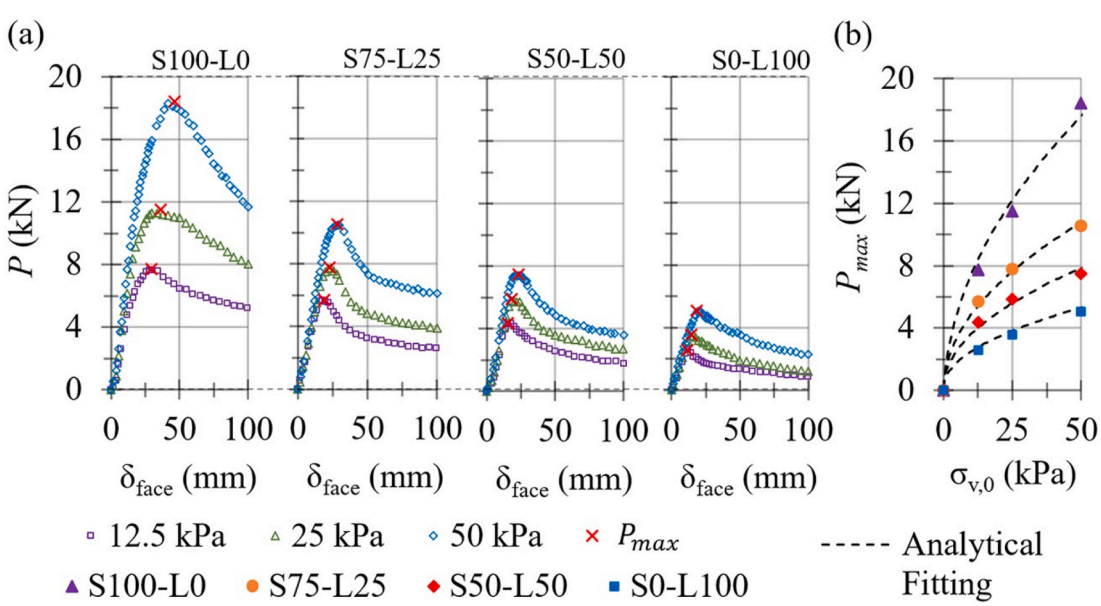

Fig. 6. Pullout test results: (a) relation between pullout forces and frontal displacements; and (b) failure envelopes and analytical fitting.

Table 4
Summary of the pullout testing results.

Properties			$\sigma_{v,0}$ (kPa)			Properties			$\sigma_{v,0}$ (kPa)		
			12.5	25	50				12.5	25	50
S100-L0	$\delta_{face,max}$ (m)		0.29	0.36	0.46	**S75-L25**	$\delta_{face,max}$ (m)		0.19	0.23	0.28
	P_{max} (kN)		7.73	11.49	18.43		P_{max} (kN)		5.70	7.77	10.55
	Stresses (kPa)	PC-1	31.48	56.07	102.46		Stresses (kPa)	PC-1	27.62	43.57	72.29
		PC-2	29.85	57.02	98.08			PC-2	24.69	42.82	72.60
		PC-3	31.08	53.41	101.57			PC-3	22.39	41.71	68.73
		PC-4	12.55	22.36	50.41			PC-4	12.20	25.41	53.07
		PC-5	12.07	21.72	49.71			PC-5	11.96	24.36	52.27
		$\sigma_{v,max}$	30.80	55.50	100.70			$\sigma_{v,max}$	24.90	42.70	71.20
		$\Delta\sigma_{v,max}$	18.30	30.50	50.70			$\Delta\sigma_{v,max}$	12.40	17.70	21.20
	f^*		2.52	1.88	1.50		f^*		1.86	1.27	0.86
	f		1.02	0.84	0.75		f		0.93	0.74	0.60
S50-L50	$\delta_{face,max}$ (m)		0.15	0.18	0.23	**S0-L100**	$\delta_{face,max}$ (m)		0.12	0.14	0.19
	P_{max} (kN)		4.37	5.88	7.48		P_{max} (kN)		2.58	3.57	5.07
	Stresses (kPa)	PC-1	22.77	36.35	64.24		Stresses (kPa)	PC-1	16.63	32.50	57.89
		PC-2	20.25	35.70	61.75			PC-2	15.84	31.26	57.06
		PC-3	21.18	34.15	57.01			PC-3	14.62	29.55	56.93
		PC-4	14.22	25.74	51.80			PC-4	11.78	23.04	47.76
		PC-5	14.88	24.21	49.69			PC-5	11.95	23.16	48.19
		$\sigma_{v,max}$	21.40	35.40	61.00			$\sigma_{v,max}$	15.70	31.10	57.30
		$\Delta\sigma_{v,max}$	8.90	10.40	11.00			$\Delta\sigma_{v,max}$	3.20	6.10	7.30
	f^*		1.43	0.96	0.61		f^*		0.84	0.58	0.41
	f		0.83	0.68	0.50		f		0.67	0.47	0.36

Note: The soil samples used for pullout testing, as indicated in Table 4, met the following criteria: water content of approximately 0.25%, the relative density of 95% ± 3% for sample S100-L0; and water content of w_{opt} ± 2%, and relative compaction of 95% ± 3% for samples S75-L25, S50-L50, and S0-L100.

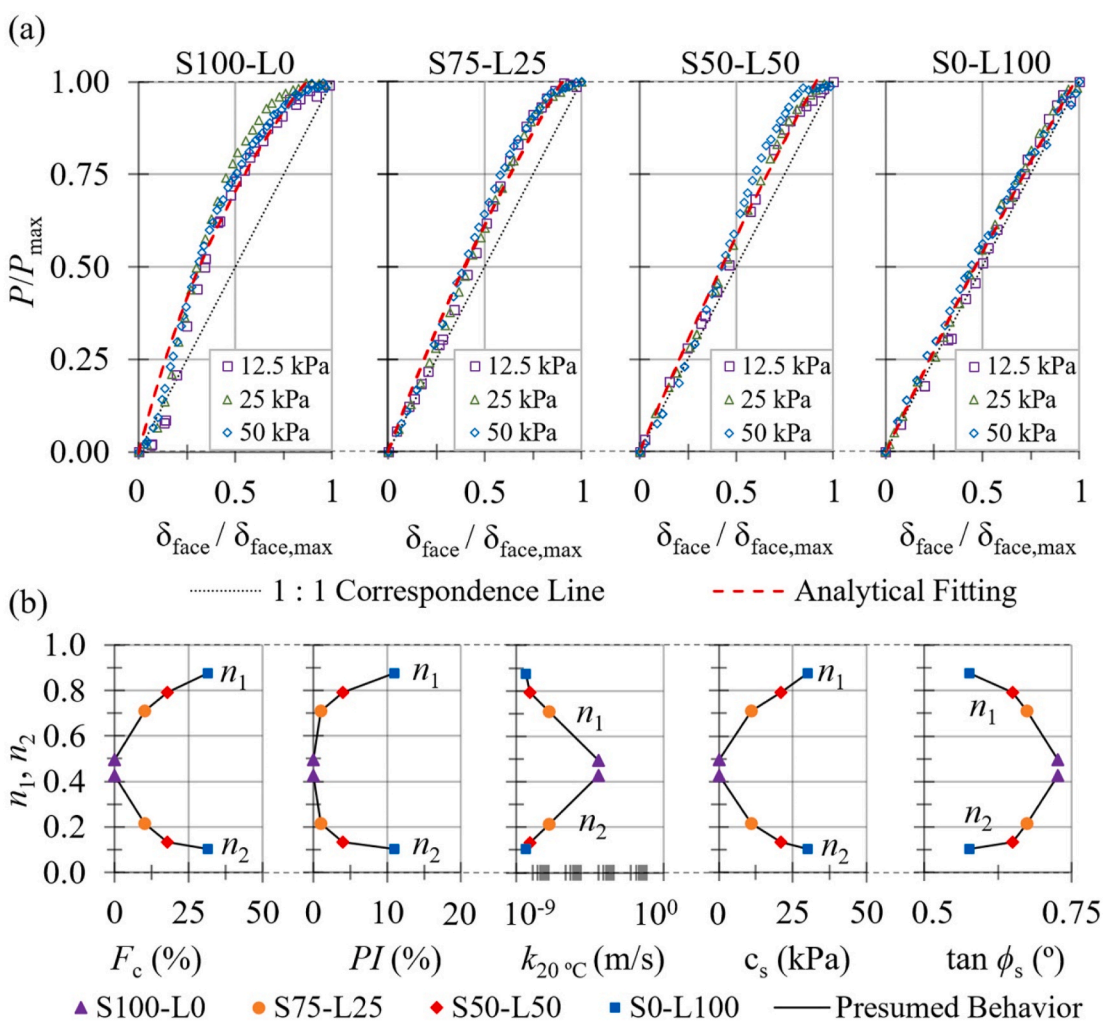

Fig. 7. Pullout resistance in dimensionless units: (a) load-displacement curves and analytical fitting; and (b) relation between fitted coefficients (n_1, and n_2) and selected geomechanical fill properties.

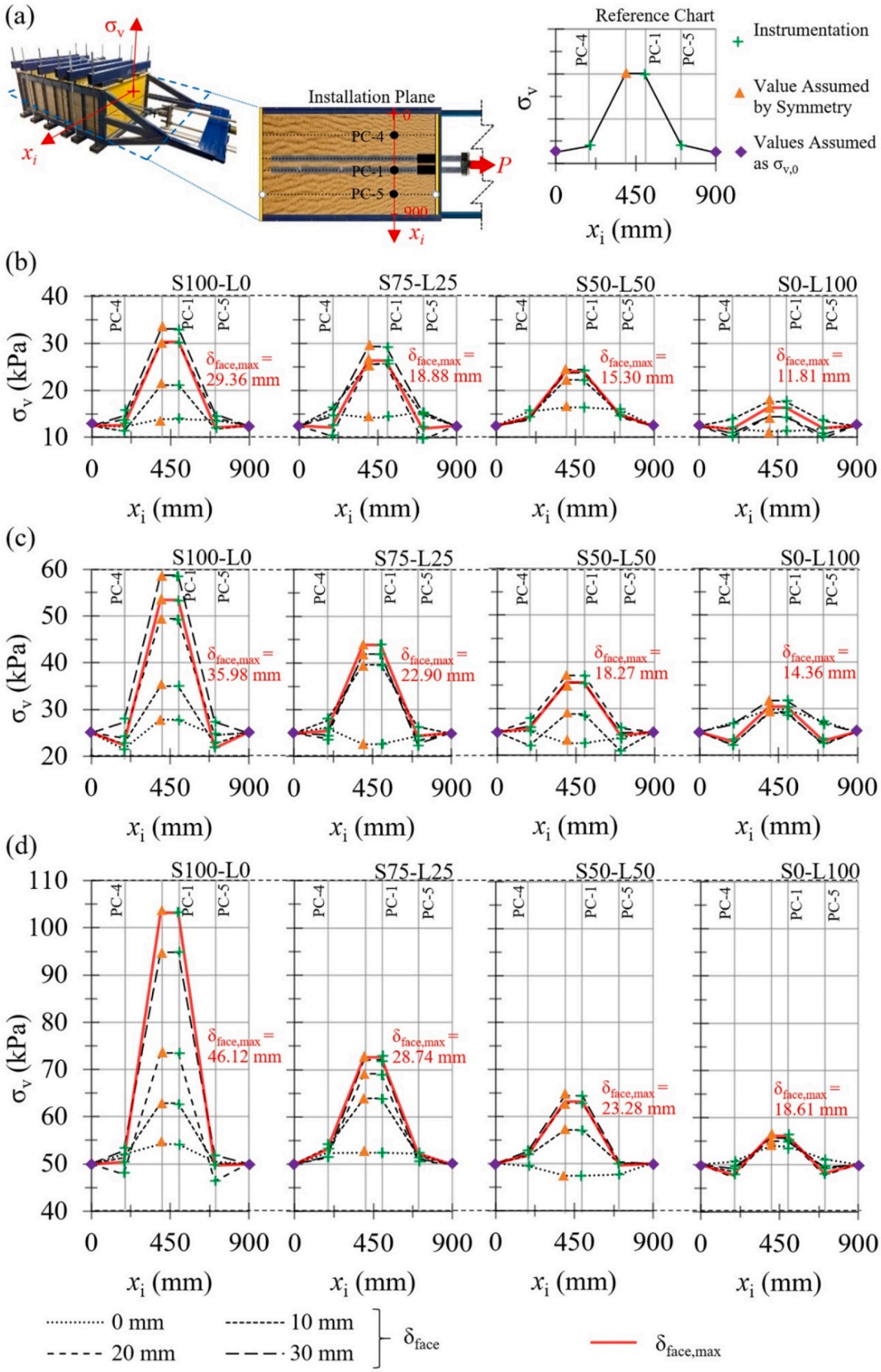

Fig. 8. Actual stresses acting within the soil (PC-4, and PC-5) and on top of the reinforcements (PC-1): (a) area of analysis; (b) $\sigma_{v,0}$ of 12.5 kPa; (c) $\sigma_{v,0}$ of 25 kPa; and (d) $\sigma_{v,0}$ of 50 kPa.

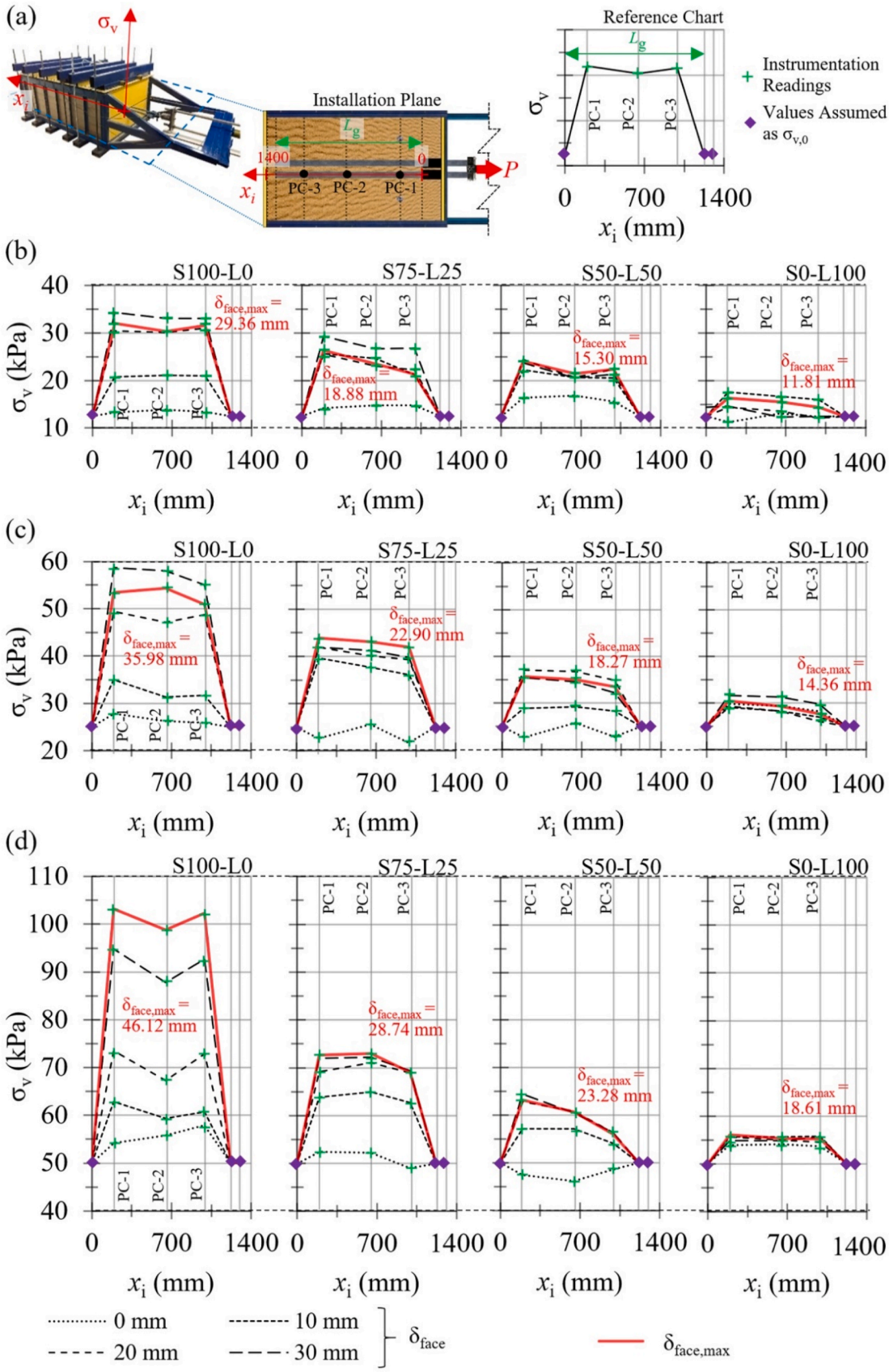

Fig. 9. Actual stresses acting on top of reinforcements (PC-1, PC-2, and PC-3): (a) area of analysis; (b) $\sigma_{v,0}$ of 12.5 kPa; (c) $\sigma_{v,0}$ of 25 kPa; and (d) $\sigma_{v,0}$ of 50 kPa.

mended by previous authors (e.g. Huang et al., 2014; Kumar and Ilamparuthi, 2020), which is representative of the stress-strain responses of cohesive soils (e.g. Kondner, 1963). This model presented strong statistical agreement ($R^2 > 95\%$) with the experimental data in the range of $0 < \delta_{face}/\delta_{face,max} \leq 1$, expressed as follows:

$$\frac{P}{P_{max}} = \frac{\delta_{face}/\delta_{face,max}}{n_1 + n_2 \times \delta_{face}/\delta_{face,max}} \tag{8}$$

where n_1 and n_2 are dimensionless model coefficients, δ_{face} is the face displacement during testing, and $\delta_{face,\ max}$ is the face displacement at failure.

Given the observed effect of fill type on pullout responses, a series of comparisons between different geomechanical properties and the fitted coefficients n_1 and n_2 [Eq. (8)] were conducted, with results shown in Fig. 7(b). It should be noted that parameter n_1 serves as a reduction factor in the referenced equation, and parameter n_2 weights the curvature of the hyperbolic function. Parameter n_1 presented a positive correlation with the fines content (the mass fraction with a diameter smaller than 0.075 mm, F_c), plasticity indices (PI), and cohesion intercepts (c_s), while the increase in permeability coefficients ($k_{20°C}$) and increase in the friction angles (tan ϕ_s) caused a decrease in the values associated with parameter n_1. Therefore, it can be presumed that an increase in the magnitude of variables typically characteristic of cohesive soils (i.e. F_c, PI, and c_s) causes a decrease in pullout effort, while an increase in the magnitude of variables characteristic of granular soils (i.e. $k_{20°C}$, and tan ϕ_s) has the opposite effect. In contrast, parameter n_2 presented the opposite behavior relative to n_1, indicating the curvature of the dimensionless load-displacement curves is affected by the geomechanical properties of the fill. The observed correlation between pullout responses and geomechanical fill properties can lead to straightforward preliminary design assumptions.

4.2. Soil stress distribution

It is important to consider that, in general, the experimental results associated with total pressure cells are considerably affected by compaction or compaction conditions of the surrounding soil. Since pullout of the reinforcements can lead to particle rearrangement at the soil-geosynthetic interface, the accuracy of readings associated with the pressure cell may be affected during testing. For these reasons, the values associated with $\Delta\sigma_{v,max}$ reported in this research may present slight variations with actual behavior.

The actual vertical stresses (σ_v) acting on top of the reinforcements (PC-1) and within the fill (PC-4, and PC-5) at the level of reinforcement are presented in Fig. 8, while the pressure cells readings considered in these analyses are summarized in Table 4. A schematic representation of the plan view is shown in Fig. 8(a), while the results of tests conducted with initial stress conditions of 12.5 kPa, 25 kPa, and 50 kPa are given in Fig. 8(b), (c), and 8(d), respectively.

It can be observed in Fig. 8(b), (c), and 8(d) that the actual stresses (σ_v) acting on the reinforcement level along axis x_i did not present significant variation relative to the initial stress conditions ($\sigma_{v,0}$) for null face displacements (δ_{face} equal to 0 mm), even though slight differences may be attributed to arching effects relative to differences in stiffness between the reinforcements and surrounding soil under steady conditions. On the other hand, the actual stresses acting on top of the reinforcements (PC-1) showed a continuous increase during pullout until failure was reached ($\delta_{face,max}$), while the actual stresses within the embankment (PC-4, and PC-5) remained almost constant. It can also be observed that the magnitude of stresses mobilized during pullout was considerably larger for the clean uniform sand (S100-L0) relative to the lateritic soil (S0-L100), while mixtures S75-L25 and S50-L50 presented intermediate behavior.

It was observed that the stresses acting on top of the reinforcements at position PC-1 were significantly larger than the stresses acting at positions PC-4 and PC-5, indicating that pullout of the reinforcement can mobilize stresses much larger than those considered in traditional design procedures. Since it was possible to capture the changes in stress distribution with the reinforcement pullout via pressure cells PC-1, PC-4, and PC-5, additional investigations were also carried out. A comparison of readings from the pressure cells installed on top of the reinforcements (PC-1, PC-2, and PC-3) is given in Fig. 9, with a schematic representation of the relevant positions shown in Fig. 9(a). Fig. 9(b), (c), and 9(d) present the results of initial stress conditions of 12.5 kPa, 25 kPa, and 50 kPa, respectively.

It can be observed in Fig. 9(b), (c), and (d) that the progressive pullout of the reinforcements caused a progressive increase in the vertical stresses acting on top of the reinforcements up to interface failure conditions. Based on the observed behavior, it was possible to estimate the actual stresses acting on the reinforcements ($\sigma_{v,max}$) according to the average readings of pressure cells PC-1, PC-2, and PC-3 under peak conditions. Accordingly, the increments in vertical stresses were determined as the difference between actual and initial stress conditions (Eq. (4)).

Fig. 10 presents the average stresses acting on top of the reinforcements and associate friction coefficients, including a comparison between local increases in vertical stresses and actual stresses (average values) with initial stress conditions [Fig. 10(a)], and correlations between f^*/f and shear strength parameters [Fig. 10(b)], and geotechnical properties and particle size coefficients [Fig. 10(c)].

It is worth noting that the different soil types induced different vertical stress responses under pullout [Fig. 10(a)]. For example, the pullout of the pair of polymeric strips within the clean uniform sand (S100-L0) resulted in larger increments in vertical stresses than those for the samples containing lateritic soil (S75-L25, S50-L50, and S0-L100). The lateritic weathered soil (S0-L100) presented poorer pullout performance relative to other samples since it does not benefit from the contribution of a compact sand dilatant skeleton, which could induce local increases in vertical stresses. It can be observed that the representation of $\Delta\sigma_{v,max}$ versus $\sigma_{v,0}$ assumes a non-linear distribution, with a shape resembling that of the failure envelopes (Fig. 6(b)), which indicates that the stress increment due to pullout has a considerable influence on interface resistance mechanisms.

It is possible to notice in Fig. 10(a) that the relationship between total stresses acting on the reinforcements at failure ($\sigma_{v,max}$) and initial stress conditions ($\sigma_{v,0}$) was linear, which presented coefficients of determination (R^2) larger than 95% with experimental data in the range of 0 kPa $< \sigma_{v,0} \leq$ 50 kPa. The linear equation used in this regard consisted of a rearrangement of the terms presented in Eq. (5), as follows:

$$\sigma_v = \frac{f^*}{f} \times \sigma_{v,0} \tag{9}$$

where the angular coefficient of the slope (β) corresponds to f^*/f (Fig. 10(a)).

The main advantage of considering the relationship f^*/f as a soil-geosynthetic interface parameter in Eq. (9) is that it can be correlated with the different geomechanical properties of fill soils, as presented in Fig. 10(b) and (c), thus providing a straightforward design tool to predict interface pullout performance. It is important to emphasize that the proposed approximation of f^*/f as a soil parameter is valid considering peak conditions and under a limited range of vertical stresses, in which a linear approximation between actual ($\sigma_{v,max}$) and initial stresses ($\sigma_{v,0}$) is reasonable. A summary of fitted parameters is presented in Table 5.

It can be assumed [Fig. 10(b)] and (c) that the geomechanical soil properties associated with granular, clean, and frictional soils, such as the internal friction angles (ϕ_s) and permeability coefficients ($k_{20°C}$), correspond with a larger component of induced stresses ($\Delta\sigma_{v,max}$), while the variables characteristic of cohesive samples, such as the cohesive intercept (c_s), liquid limits (w_L), plasticity indices (PI), fines content (the mass fraction with a diameter smaller than 0.075 mm, denoted as F_c),

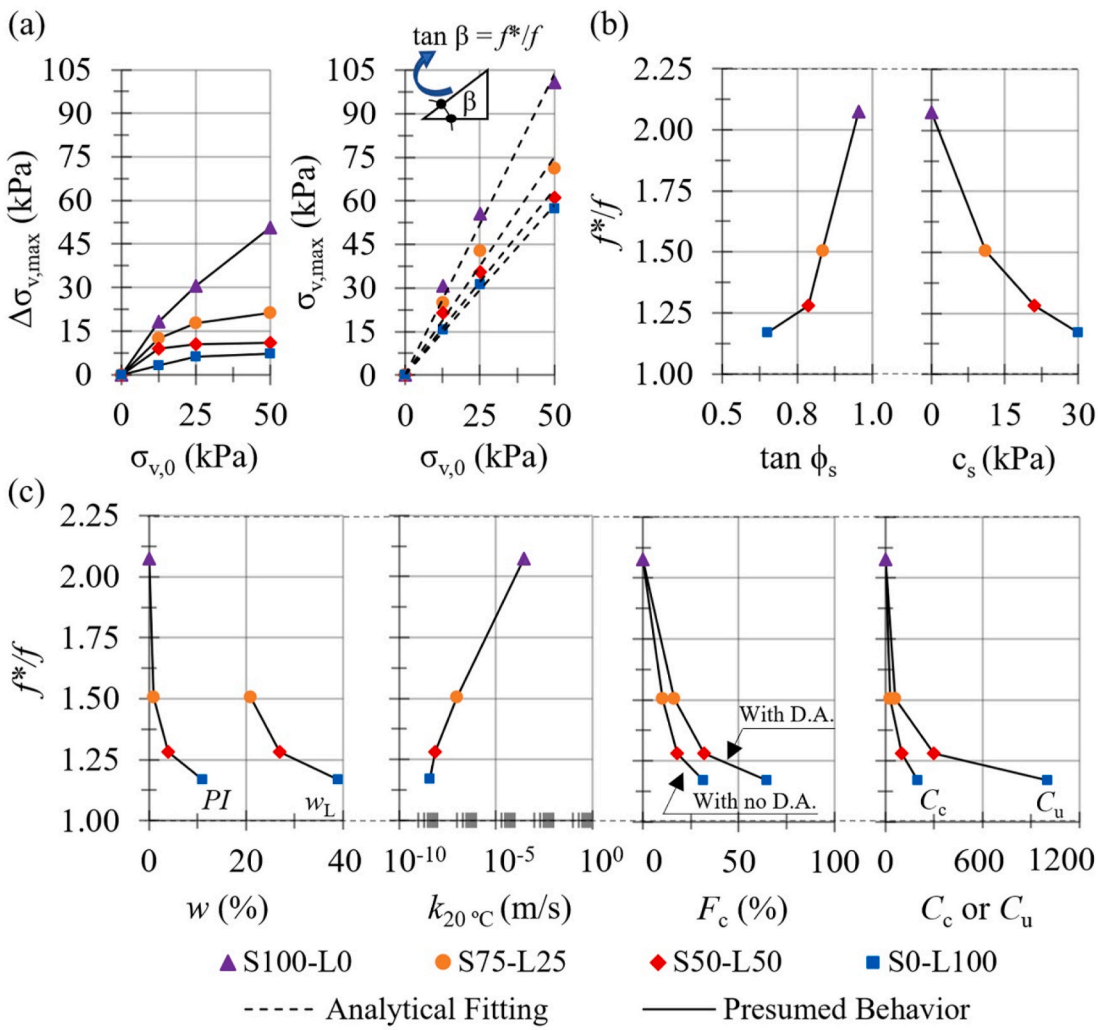

Fig. 10. Evaluation of stress configuration and associate friction coefficients: (a) increment of vertical stresses due to pullout at failure; (b) relationship between f^*/f and shear strength parameters; and (c) relationship between f^*/f and geotechnical properties and particle size coefficients.

Table 5
Analytical models used to represent the apparent and actual friction coefficients, along with values of the fitted variables.

Model	Ref.	Eq.	Functions	Var.	Soil Type			
					S100-L0	S75-L25	S50-L50	S0-L100
MD-1	a	(10)–(11)	f^* = function (f_0, f_1, $\sigma_{v,0}$)	f_0	1.10	1.02	0.89	0.79
				f_1	0.58	0.54	0.52	0.46
MD-2	b	(12)	f^* = function (α, f_b, $\phi_{s,sec}$, $\sigma_{v,0}$)	α	1.00	1.00	1.00	1.00
				f_b	1.80	1.55	1.32	0.99
MD-3	c	(13)	f^* = function (α, r_1, r_2, $\phi_{s,sec}$, $\sigma_{v,0}$)	α	1.00	1.00	1.00	1.00
				r_1	−1.11	−4.42	−7.10	−11.85
				r_2	1.60	5.35	9.13	18.11
MD-4	c	(14)	f^* = function (α, s_1, s_2, $\phi_{sg,sec}$, $\sigma_{v,0}$)	α	1.00	1.00	1.00	1.00
				s_1	−2.29	−6.44	−15.71	−11.85
				s_2	3.86	9.50	24.00	18.11
MD-5	d	(15)–(16)	f^* = function (f_0, f_1, c, $C(F_c)$, $\sigma_{v,0}$)	f_0	1.50	1.50	1.50	1.50
				f_1	0.50	0.50	0.50	0.50
				c	2.30	2.30	2.30	2.30
				$C(F_c)$	2.20	1.25	0.95	0.76
MD-6	e	(15)	f^* = function (f_0, f_1, c, C, $\sigma_{v,0}$)	f_0	1.50	1.50	1.50	1.50
				f_1	0.50	0.50	0.50	0.50
				c	2.30	2.30	2.30	2.30
				C	1.89	1.30	0.98	0.60
MD-7	–	(6)-(7)-(9)-(17)	f and f^* = function (f^*/f)	f^*/f	2.07	1.51	1.28	1.17

References: [a] NF P94-270 (2009), [b] Elias et al. (2001), [c] Adapted from Elias et al. (2001), [d] Miyata et al. (2019), and [e] Adapted from Miyata et al. (2019).

and other soil constants (i.e. C_c, C_u), were correlated with lower components of stresses induced by pullout ($\Delta\sigma_{v,\ max}$).

5. Prediction of interface pullout resistance

A summary of the correlations developed in this research is presented in Table 5, along with the values of the fitted variables. A discussion of model assumptions is presented in this section, followed by comparisons between experimental and predicted values.

5.1. Analytical models

The conventional design procedures used for reinforced soil structures are based on the following bilinear function, which is used to predict pullout responses (e.g. Elias et al., 2001):

$$f^* = f_0 \times \left(1 - \frac{z}{z_0}\right) + f_1 \times \left(\frac{z}{z_0}\right) \quad for\ \ z \le z_0 \tag{10}$$

$$f^* = f_1 \quad for\ \ z > z_0 \tag{11}$$

where z is the depth of installation, calculated as σ_{v0}/γ_{nat} in this research, z_0 is the break-point depth (assumed as 6 m), and f_0 is the maximum value for f^* and f_1 is the minimum value for f^*.

The French code (NF P94-270, 2009) can be used as a reference for the design of retaining walls reinforced with polymeric strips, providing default values for f_0 and f_1 in Eq. (10) and Eq. (11). The default values assumed by the friction coefficients range from 1.0 to 2.5 when considering f_0, and from $0.8 \times \tan\phi_s$ to $\tan\phi_s$, with ϕ_s corresponding to the internal soil friction angle, when considering f_1. As indicated in Table 5, the analytical model denoted as MD-1 refers to Eqs. (10) and (11), with f_0 and f_1 assuming the values suggested by the French code (NF P94-270, 2009).

As previously discussed, stress levels play an important role in the mechanisms of shear resistance, especially under low confining pressures. Concerns related to the non-linearity of stress configuration are partially addressed by model MD-1 (Table 5), which assumes a bilinear configuration of friction coefficients depending on the depth of reinforcement installation. However, friction behavior is dependent on the actual stresses acting on the reinforcement level, which are known to assume a non-linear configuration over different confinement levels (e.g. Schlosser and Bastick, 1991).

Attempts to represent the apparent friction coefficients (f^*) as a function of the internal shear strength have been widely discussed in the technical literature (e.g. Elias et al., 2001). In this context, the following equation has been used to estimate f^* as a fraction of the friction angles (e.g. Elias et al., 2001; Moraci and Recalcati, 2006):

$$f^* = \propto \times f_b \times \tan\phi_{s,sec} \tag{12}$$

where α is the scale effect correction factor, f_b is the pullout interaction coefficient, and $\phi_{s,sec}$ is the secant soil friction angle.

The model denoted as MD-2 in Table 5 refers to the secant component of soil friction angles ($\phi_{s,sec}$). This alternative is particularly useful to represent friction angles as a function of the vertical stresses acting on the reinforced plane. Despite considering the friction angles as a function of the initial vertical stresses, it is important to observe that Eq. (12) assumes a linear relationship between f^* and $\tan\phi$ in which $\propto \times f_b$ denotes the angular coefficient of this linear equation.

In this context, a series of trials conducted in the current research indicated that the use of a linear equation to represent f^* versus $\tan\phi_{s,sec}$ may not be the most representative design assumption. Consequently, new equations are being proposed in this paper to consider the non-linearity between f^* and $\tan\phi_{s,sec}$, and between f^* and $\tan\phi_{sg,sec}$, which are expressed as follows:

$$f^* = \propto \times e^{\left(r_1 + r_2 \times \tan\phi_{s,sec}\right)} \tag{13}$$

where r_1 and r_2 are dimensionless model coefficients.

$$f^* = \propto \times e^{\left(s_1 + s_2 \times \tan\phi_{sg,sec}\right)} \tag{14}$$

where s_1 and s_2 are dimensionless model coefficients.

The method of prediction expressed by Eq. (13) is denoted as MD-3 in Table 5, while Eq. (14) is indicated as the method of prediction MD-4 in Table 5.

Previous works in the technical literature have also attempted to provide consistent methods of representation of the f^* over different confinements, considering both metallic (Miyata and Bathurst, 2012) and polymeric (Miyata et al., 2019) strips. The following analytical equations were proposed by Miyata et al. (2019) to predict pullout resistance considering different types of materials and fines content (the mass fraction with a diameter smaller than 0.075 mm, denoted as F_c):

$$f^* = f_1 + \frac{f_0 - f_1}{e^{c \times \left(\frac{\sigma_{v,0}}{p_a}\right)}} \tag{15}$$

$$C \cong C(F_c) = C_1 + \frac{C_0 - C_1}{e^{\chi \times F_c}} \tag{16}$$

where c, C_0, C_1, and χ are dimensionless coefficients; p_a is the atmospheric pressure (101 kPa); and C is the correction factor applied to Eq. (15), which can be approximated by coefficient $C(F_c)$ considering the influence of fines content (the mass fraction with a diameter smaller than 0.075 mm).

The method of prediction proposed by Miyata et al. (2019) is denoted as MD-5 in Table 5, allowing the prediction of f^* as a function of the fines content ($C(F_c)$) and considering polymeric strips. It should be noted that the actual correction factor C applied in Eq. (15) is not necessarily limited by the fines content (the mass fraction with a diameter smaller than 0.075 mm) since it can be expressed in terms of other geomechanical properties. Thus, in this research the best fitting correction factors C were calibrated for each data set, facilitating several correlations with additional geomechanical fill properties as subsequently discussed in this paper. This calibrated model is referred to as MD-6 in Table 5.

The last model studied in this investigation is denoted as MD-7 in Table 5 and was determined based on the pullout results described herein. This prediction method can be briefly described as follows: (*i*) the maximum pullout loads (P_{max}) determined experimentally are used to calibrate the model variables l_1 and l_2 in Eq. (7), thus allowing the prediction of values assumed by the variables P_{max} *versus* $\sigma_{v,0}$ in the considered range of initial vertical stresses; (*ii*) the apparent friction coefficients (f^*) are calculated over the same range of initial vertical stresses considering the values assumed by P_{max} in Eq. (6); (*iii*) the relation f^*/f is estimated based on the geomechanical fill properties [Fig. 10(b) and (c)]; and (*iv*) the actual friction coefficients (f) are calculated considering the estimative of f^*/f and according to the following equation:

$$f = \frac{P_{max}}{2 \times L_g \times W_g \times \sigma_{v,max}} = \frac{P_{max}}{2 \times L_g \times W_g \times \sigma_{v,0} \times \left(\frac{f^*}{f}\right)} \tag{17}$$

where the f^*/f relation is estimated based on the geomechanical fill properties [Fig. 10(b) and (c)].

5.2. Comparisons between measured and predicted results

Measured and predicted values are presented in this section aiming at supporting a discussion on model assumptions and their significance from the design perspective. The results considering the apparent

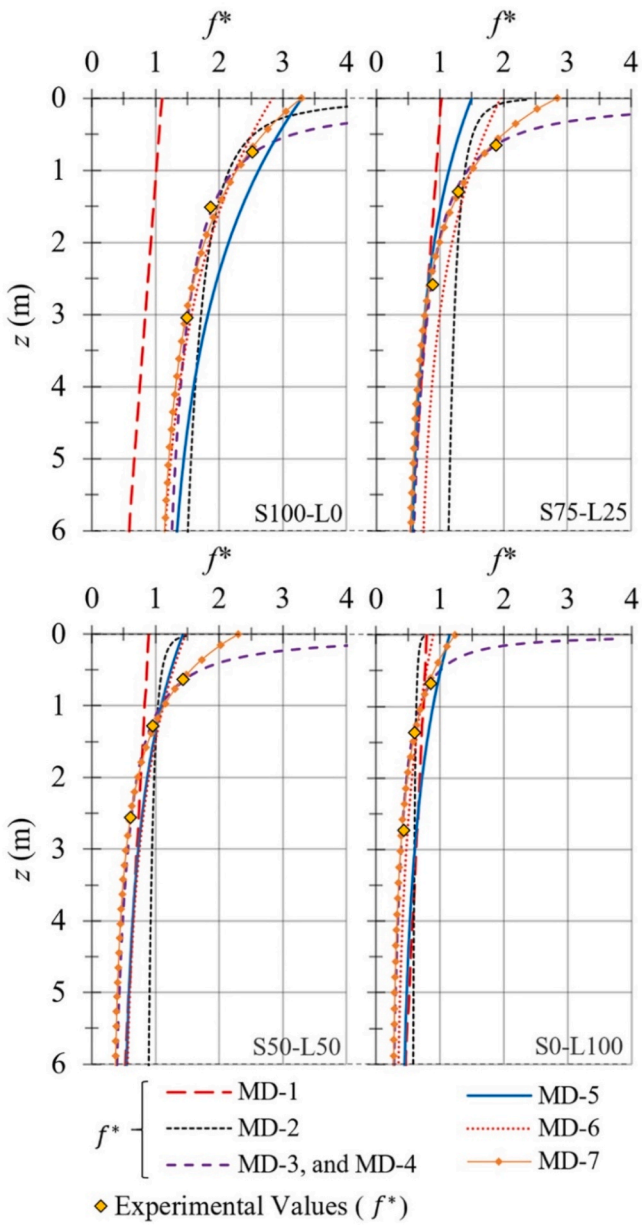

Fig. 11. Comparison between experimental and predicted results for apparent friction coefficients.

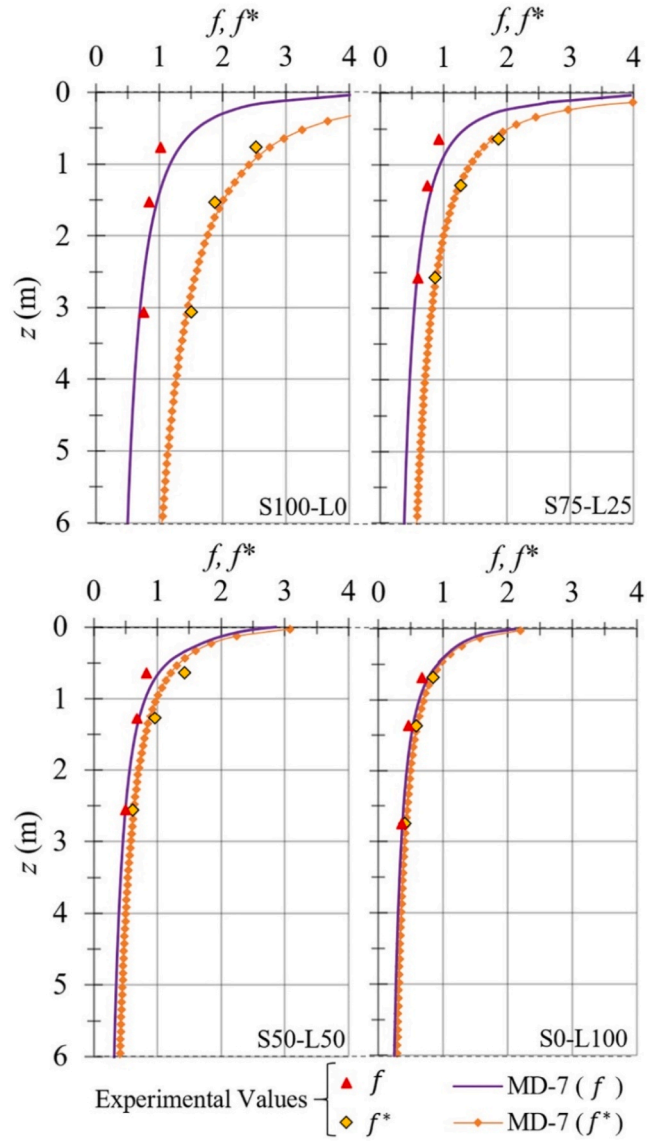

Fig. 12. Comparison between experimental and predicted results for actual friction coefficients.

friction coefficients are presented in Fig. 11, and a comparison between apparent and real friction coefficients is presented in Fig. 12.

It is worth mentioning that the default model MD-1 (NF P94-270, 2009) is inherently associated with conservative design assumptions considering it was established in prior decades and aimed at representing a wide range of conditions, which was also reflected in the selected statistical boundaries. It can be observed in Fig. 11 that the predictions with model MD-1 were conservative with the actual pullout behavior for the clean uniform sand (S100-L0), while a better agreement was observed with the cohesive samples (S75-L25, S50-L50, and S0-L100). Predictions associated with model MD-1 did not present considerable differences between the different types of soils, even though they presented very distinct geotechnical behavior amongst themselves.

Models MD-2 (Elias et al., 2001), MD-3, and MD-4 (adapted from Elias et al., 2001) had the advantage of allowing the calibration of model variables based on pullout test and direct shear test results [Eq. (12), Eq. (13), and Eq. (14)]. Model MD-2 demonstrated poorer performance relative to models MD-3 and MD-4 since the former two models consider the use of a non-linear equation to describe the relationship between f^* and friction [Eqs. (13) and (14)], while MD-2 considers a linear relationship between these variables [Eq. (12)]. Considerable differences were not observed between models MD-3 and MD-4, supporting the illustration of a single curve in Fig. 11.

Model MD-5 was found to provide more consistent predictions for pullout friction with the previously discussed models. Model MD-5 was able to better capture the nuances of the geotechnical behavior based on the type of soil and fines content (the mass fraction with a diameter smaller than 0.075 mm), especially for the clean uniform sand (S100-L0). It is important to note that the fines content considered in Eq. (16) corresponded to hydrometer tests without the use of a D.A. (ASTM D4221-18, 2018), in contrast to the original method proposed by Miyata et al. (2019). These results indicate that prediction methods incorporating variables related to the geomechanical behavior of the soil can provide more reliable sources of information, especially when considering the particularities of cohesive tropical soils. The advantages of model MD-5 were also reflected in the predictions of model MD-6, in which the correction factor C [Eq. (15)] was calibrated based on pullout tests.

A comparison between apparent and actual friction coefficients determined using model MD-7 are shown in Fig. 12, where it can be observed that the gap between apparent and actual friction coefficients decreased as the lateritic soil content increased. This behavior reflects pullout resistance failure envelopes [Fig. 6(b)], in which an increase in lateritic soil caused a decrease in resistance, along with the differences in stresses induced during pullout (Fig. 9). The shape of the dimensionless load-displacement curves [Fig. 7(a)] was also observed to be consistent with these results. Based on these results, samples containing less than 25% lateritic soil were considered adequate for use as partial replacement of the clean uniform sand in retaining walls reinforced with polymeric strips.

6. Summary and conclusions

This paper presented a study on the use of coarse- and fine-grained tropical soils as fills in retaining walls reinforced with polymeric strips. The experimental component of this evaluation included the geomechanical characterization of these soils and large-scale pullout tests, followed by an analytical component that provided insight into the factors affecting interface shear strength. The most relevant lessons learned are as follows:

- Local increases in vertical stresses induced during pullout of polymeric strips were found to considerably impact the friction coefficients assumed by conventional approaches. The relationship between actual and initial stresses was found to be linear, so the resulting angular coefficient (i.e. f^*/f) may be incorporated into the design based on readily available geomechanical properties, such as in model MD-7 presented in this paper.
- The actual stresses acting on the reinforcements were found to increase significantly relative to initial stress conditions during pullout of clean uniform sand and mixtures with a lateritic weathered soil fraction below 25%.
- The particular characteristics of the lateritic weathered soil were found to affect pullout resistance considerably. For example, the presence of sesquioxides caused the formation of micro-aggregations that were found to lead to poor pullout response. The sesquioxides also added interparticle bounding to sand particles, resulting in a decreased dilatant behavior that negatively influenced the pullout resistance.
- The shape of dimensionless load-displacement curves could be correlated with geomechanical fill properties. In particular, the level of frontal displacement required to achieve a certain percentage of the pullout resistance was found to be comparatively lower for clean and granular sands than for fine-grained materials, ultimately resulting in comparatively larger mobilization of stresses within the granular materials.
- The analytical method proposed by Miyata et al. (2019) was found to be a particularly useful tool to predict the pullout responses in terms of apparent friction coefficients (f^*) of polymeric strips embedded in coarse- and fine-grained tropical soils, especially after calibration with experimental results. Accordingly, complementary analyses with the analytical model presented in this research (denoted as MD-7) enables the prediction of the actual friction coefficients (f) by considering the f^*/f relation as an input argument.

Sand-lateritic soil mixtures can provide a variety of technical and economic opportunities for use in tropical regions, such as the central region of Brazil. Overall, the interface frictional behavior of retaining walls reinforced with polymeric strips was significantly affected by the geomechanical properties of fill soils. The inherent characteristics of lateritic weathered soils did not compromise the pullout resistance of sand-lateritic soil mixtures that kept the lateritic soil fraction below a threshold. This provides innovative ranges of application for lateritic soils in the construction of retaining structures reinforced with polymeric straps.

Declaration of competing interest

The authors declare that they have no known competing financial interests or personal relationships that could have appeared to influence the work reported in this paper.

Acknowledgements

The authors gratefully acknowledge the funding provided by the Brazilian National Council for Scientific and Technological Development (CNPq), the Coordination for the Improvement of Higher Education Personnel (CAPES), and the Federal District Research Foundation (FAP/DF) to conduct the various components of this research, including project number 471043/2013-3, sponsored by CNPq. The authors would also like to thank the anonymous reviewers whose comments and suggestions helped improve and clarity this manuscript.

References

AASHTO, 2017. In: LRFD Bridge Design Specifications, eighth ed. American Association of State Highway and Transportation Officials, Washington, DC, USA.

Abdelouhab, A., Dias, D., Freitag, N., 2010. Physical and analytical modelling of geosynthetic strip pull-out behavior. Geotext. Geomemb. 28 (1), 44–53. https://doi.org/10.1016/j.geotexmem.2009.09.018.

Abdelouhab, A., Dias, D., Freitag, N., 2011. Numerical analysis of the behaviour of mechanically stabilized earth walls reinforced with different types of strips. Geotext. Geomemb. 29 (2), 116–129. https://doi.org/10.1016/j.geotexmem.2010.10.011.

Abd, A.H., Utili, S., 2017. Design of geosynthetic-reinforced slopes in cohesive backfills. Geotext. Geomemb. 45 (6), 627–641. https://doi.org/10.1016/j.geotexmem.2017.08.004.

Abdi, M.R., Arjomand, M.A., 2011. Pullout tests on clay reinforced with geogrid encapsulated in thin layers of sand. Geotext. Geomemb. 29 (6), 588–595. https://doi.org/10.1016/j.geotexmem.2011.04.004.

Abdi, M.R., Mirzalifar, H., 2017. Experimental and PIV evaluation of grain size and distribution on soil-geogrid interactions in pullout tests. Soils Found 57 (6), 1045–1058. https://doi.org/10.1016/j.sandf.2017.08.030.

Alfaro, M.C., Hayashi, S., Miura, N., Watanabe, K., 1995. Pullout interaction mechanism of geogrid strip reinforcement. Geosynt. Int. 2 (4), 679–698. https://doi.org/10.1680/gein.2.0030.

Araujo, G.L.S., Palmeira, E.M., Cunha, R.P., 2009. Behaviour of geosynthetic-encased granular columns in porous collapsible soil. Geosynt. Int. 16 (6), 433–451. https://doi.org/10.1680/gein.2009.16.6.433.

Araujo, G.L.S., Moreno, J.A.S., Zornberg, J.G., 2021. Shear behavior of mixtures involving tropical soils and tire shreds. Const. Building Mat. 276, 122061. https://doi.org/10.1016/j.conbuildmat.2020.122061.

ASTM D421-85, 2007. In: Standard Practice for Dry Preparation of Soil Samples for Particle-Size Analysis and Determination of Soil Constants. The American Society for Testing and Materials, p. 2. https://doi.org/10.1520/D0421-85R07.

ASTM D422-63e2, 2007. In: Standard Test Method for Particle-Size Analysis of Soils. The American Society for Testing and Materials, p. 8. https://doi.org/10.1520/D0422-63R07E02.

ASTM D3080/D3080M-11, 2011. In: Standard Test Method for Direct Shear Test of Soils under Consolidated Drained Conditions. The American Society for Testing and Materials, p. 9. https://doi.org/10.1520/D3080_D3080M-11.

ASTM D6706-01, 2013. In: Standard Test Method for Measuring Geosynthetic Pullout Resistance in Soil. The American Society for Testing and Materials, p. 7. https://doi.org/10.1520/D6706-01R13.

ASTM D698-12, 2021. Standard Test Methods for Laboratory Compaction Characteristics of Soil Using Standard Effort (12,400 ft-lbf/ft^3 (600 kN-m/m^3)). The American Society for Testing and Materials, p. 13. https://doi.org/10.1520/D0698-12R21.

ASTM D854-14, 2014. In: Standard Test Method for Specific Gravity of Soil Solids by Water Pycnometer. The American Society for Testing and Materials, p. 8. https://doi.org/10.1520/D0854-14.

ASTM D4253-16e1, 2016. In: Standard Test Methods for Maximum Index Density and Unit Weight of Soils Using a Vibratory Table. The American Society for Testing and Materials, p. 14. https://doi.org/10.1520/D4253-16E01.

ASTM D4254-16, 2016. In: Standard Test Methods for Minimum Index Density and Unit Weight of Soils and Calculation of Relative Density. The American Society for Testing and Materials, p. 9. https://doi.org/10.1520/D4254-16.

ASTM D5084-16a, 2016. In: Standard Test Methods for Measurement of Hydraulic Conductivity of Saturated Porous Materials Using a Flexible Wall Permeameter. The American Society for Testing and Materials, p. 24. https://doi.org/10.1520/D5084-16A.

ASTM D4287-17e1, 2017. In: Standard Practice for Classification of Soils for Engineering Purposes (Unified Soil Classification System). The American Society for Testing and Materials, p. 10. https://doi.org/10.1520/D2487-17E01.

ASTM D4318-17e1, 2017. In: Standard Test Methods for Liquid Limit, Plastic Limit, and Plasticity Index of Soils. The American Society for Testing and Materials, p. 20. https://doi.org/10.1520/D4318-17E01.

ASTM D4221-18, 2018. In: Standard Test Method for Dispersive Characteristics of Clay Soil by Double Hydrometer. The American Society for Testing and Materials, p. 5. https://doi.org/10.1520/D4221-18.

ASTM D2434-19, 2019. In: Standard Test Method for Permeability of Granular Soils (Constant Head). The American Society for Testing and Materials, p. 6. https://doi.org/10.1520/D2434-19.

ASTM D5321/D5321M-20, 2020. In: Standard Test Method for Determining the Shear Strength of Soil-Geosynthetic and Geosynthetic-Geosynthetic Interfaces by Direct Shear. The American Society for Testing and Materials, p. 12. https://doi.org/10.1520/D5321_D5321M-20.

Bathurst, R.J., Ezzein, F.M., 2016. Geogrid pullout load-strain behaviour and modelling using a transparent granular soil. Geosynt. Int. 23 (4), 271–286. https://doi.org/10.1680/jgein.15.00051.

Berg, R.R., Christopher, B.R., Samtani, N.C., 2009. Design and Construction of Mechanically Stabilized Earth Walls and Reinforced Soil Slopes, Volume I. U.S. Department of Transportation, Federal Highway Administration, National Highway Institute, Washington, D.C.

Bolton, M.D., 1986. The strength and dilatancy of sands. Géotechnique 36 (1), 65–78. https://doi.org/10.1680/geot.1986.36.1.65.

Cardile, G., Gioffrè, D., Moraci, N., Calvarano, L.S., 2017. Modelling interference between geogrid bearing members under pullout loading conditions. Geotext. Geomemb. 45 (3), 169–177. https://doi.org/10.1016/j.geotexmem.2017.01.008.

Catt, J.A., 1990. Tropical residual soils. Geological society engineering group working party report. Q. J. Eng. Geology Hydrogeology 23 (1), 4–101. https://doi.org/10.1144/GSL.QJEG.1990.023.001.01.

Chen, Y., Gao, Y., Yang, S., Zhang, F., 2018. Required unfactored geosynthetic strength of three-dimensional reinforced soil structures comprised of cohesive backfills. Geotext. Geomemb. 46 (6), 860–868. https://doi.org/10.1016/j.geotexmem.2018.08.004.

Cui, X.-Z., Wang, Y.-L., Liu, K.-W., Wang, X.-Z., Jin, Q., Zhao, M.-L., Cui, S.-Q., 2019. A simplified model for evaluating the hardening behaviour of sensor-enabled geobelts during pullout tests. Geotext. Geomemb. 47 (3), 377–388. https://doi.org/10.1016/j.geotexmem.2019.01.007.

Dai, B., Yang, J., Luo, X., 2015. A numerical analysis of the shear behavior of granular soil with fines. Particuology 21 (1), 160–172. https://doi.org/10.1016/j.partic.2014.08.010.

Elias, V., Christopher, B.R., Berg, R.R., 2001. Mechanically Stabilized Earth Walls and Reinforced Soil Slopes Design and Construction Guidelines. U.S. Dept. of Transp., Federal Highw. Adm., p. 394

Ezzein, F.M., Bathurst, R.J., 2014. A new approach to evaluate soil-geosynthetic interaction using a novel pullout test apparatus and transparent granular soil. Geotext. Geomemb. 42 (3), 246–255. https://doi.org/10.1016/j.geotexmem.2014.04.003.

Gálvez-Martos, J.-L., Styles, D., Schoenberger, H., Zeschmar-Lahl, B., 2018. Construction and demolition waste best management practice in Europe. Resources. Conservation & Recycling 136 (1), 166–178. https://doi.org/10.1016/j.resconrec.2018.04.016.

Gao, J.L., Zhang, M.X., Zhang, W.J., 2010. Interface frictional property between sand and geomembrane. In: Chen, Y., Zhan, L., Tang, X. (Eds.), Advances in Environmental Geotechnics. Springer, Berlin. https://doi.org/10.1007/978-3-642-04460-1_104.

Georgiou, I., Loli, M.m, Kourkoulis, R., Gazetas, G., 2020. Pullout of steel grids in dense sand: experiments and design insights. J. Geot. Geoenviron. Eng. 146 (10), 1–19. https://doi.org/10.1061/(ASCE)GT.1943-5606.0002358.

Gidigasu, M.D., 1972. Mode of formation and geotechnical characteristics of laterite materials of Ghana in relation to soil forming factors. Eng. Geology 6 (2), 79–150. https://doi.org/10.1016/0013-7952(72)90034-8.

Huang, C.-C., Hsieh, H.-Y., Hsieh, Y.-L., 2014. Hyperbolic models for 2-D backfill and reinforcement pullout. Geosynt. Int. 21 (3), 168–178. https://doi.org/10.1680/gein.14.00007.

Jewell, R.A., 1989. Direct shear tests on sands. Géotechnique 39 (2), 309–322. https://doi.org/10.1680/geot.1989.39.2.309.

Kayadelen, C., Önal, T.O., Altay, G., 2018. Experimental study on pull-out response of geogrid embedded in sand. Measurement 117 (1), 390–396. https://doi.org/10.1016/j.measurement.2017.12.024.

Khedkar, M.S., Mandal, J.N., 2009. Pullout behavior of cellular reinforcements. Geotext. Geomemb. 27 (4), 262–271. https://doi.org/10.1016/j.geotexmem.2008.12.003.

Kido, R., Kimura, M., 2021. Investigation of soil deformation characteristics during pullout of a ribbed reinforcement using X-ray micro CT. Soils Found 26. https://doi.org/10.1016/j.sandf.2021.01.013 (in press).

Klein, C., Hurlbut, C.S., 1993. Manual of Mineralogy (After James D. Dana), twenty-first ed. John Wiley & Sons, New York, USA, p. 681. https://doi.org/10.1002/gj.3350300114.

Kondner, R.L., 1963. Hyperbolic stress-strain response: cohesive soils. ASCE J. Soil Mechanics Found. Eng. Division 89 (1), 115–143. https://doi.org/10.1061/JSFEAQ.0000479.

Kumar, V.K., Ilamparuthi, K., 2020. Performance of anchor in sand with different forms of geosynthetic reinforcement. Geosynt. Int. 27 (5), 503–522. https://doi.org/10.1680/jgein.20.00013.

Lajevardi, S.H., Dias, D., Racinais, J., 2013. Analysis of soil-welded steel mesh reinforcement interface interaction by pull-out tests. Geotext. Geomemb. 40 (1), 48–57. https://doi.org/10.1016/j.geotexmem.2013.08.002.

Loli, M., Georgiou, I., Kourkoulis, R., Gelagoti, F., 2018. Pull-out testing of steel reinforced earth systems: modeling in view of soil dilation and boundary effects. In: Physical Modelling in Geotechnics, first ed. CRC Press, p. 5. https://doi.org/10.1201/9780429438646-98.

Lo Presti, D.C.F., Pedroni, S., Crippa, V., 1992. Maximum dry density of cohesionless soils by pluviation and by ASTM D4253-83: a comparative study. Geot. Testing J. 15 (2), 180–189. https://doi.org/10.1520/GTJ10239J.

Luo, Y., Leshchinsky, D., Rimoldi, P., Lugli, G., Xu, C., 2015. Instrumented mechanically stabilized earth wall reinforced with polyester straps. Transp. Research Record 2511 (1), 9–17. https://doi.org/10.3141/2511-02.

Mahalinga-Iyer, Y., Williams, D.J., 1994. Consolidation and shear strength properties of a lateritic soil. Eng. Geology 38 (1–2), 53–63. https://doi.org/10.1016/0013-7952(94)90024-8.

Miyata, Y., Bathurst, R.J., 2012. Analysis and calibration of default steel strip pullout models used in Japan. Soils Found 52 (3), 481–497. https://doi.org/10.1016/j.sandf.2012.05.007.

Miyata, Y., Bathurst, R.J., Allen, T.M., 2019. Calibration of PET strap pullout models using a statistical approach. Geosynt. Int. 26 (4), 413–427. https://doi.org/10.1680/jgein.19.00026.

Mitchell, J.K., Zornberg, J.G., 1995. Reinforced soil structures with poorly draining backfills. Part II: case histories and applications. Geosynt. Int. 2 (1), 265–307. https://doi.org/10.1680/gein.2.0011.

Moraci, N., Cardile, G., 2009. Influence of cyclic tensile loading on pullout resistance of geogrids embedded in a compacted granular soil. Geotext. Geomemb. 27 (6), 475–487. https://doi.org/10.1016/j.geotexmem.2009.09.019.

Moraci, N., Recalcati, P., 2006. Factors affecting the pullout behaviour of extruded geogrids embedded in a compacted granular soil. Geotext. Geomemb. 24 (4), 220–242. https://doi.org/10.1016/j.geotexmem.2006.03.001.

NF P94-270, 2009. Geotechnical Design – Retaining Structures – Reinforced and Soil Nailing Structures. Association Française de Normalisation, p. 205 (in French).

Ng, C.W.W., Akinniyi, D.B., Zhou, C., Chiu, C.F., 2019. Comparisons of weathered lateritic, granitic and volcanic soils: compressibility and shear strength. Eng. Geology 249 (1), 235–240. https://doi.org/10.1016/j.enggeo.2018.12.029.

Noorzad, A., Badakhshan, E., 2017. Investigations on pullout behavior of geogrid-granular trench using CANAsand constitutive model. J. Rock Mec. Geot. Eng. 9 (4), 726–740. https://doi.org/10.1016/j.jrmge.2017.03.013.

Palmeira, E.M., 1987. The Study of Soil-Reinforcement Interaction by Means of Large Scale Laboratory Tests. Ph.D. thesis. University of Oxford, Magdalen College, England, p. 237.

Palmeira, E.M., 1996. Design and Construction of a Large-Scale Pullout Box. Research Report. The University of Brasilia, Brazil (in Portuguese).

Palmeira, E.M., 2004. Bearing force mobilization in pull-out tests on geogrids. Geotext. Geomemb. 22 (6), 481–509. https://doi.org/10.1016/j.geotexmem.2004.03.007.

Palmeira, E.M., 2009. Soil-geosynthetic interaction: modelling and analysis. Geotext. Geomemb. 27 (5), 368–390. https://doi.org/10.1016/j.geotexmem.2009.03.003.

Pierozan, R.C., 2018. Interface Resistance of Metallic and Polymeric Strips Embedded in Different Soils. Ph.D. thesis. University of Brasilia, Brazil, p. 287 (in Portuguese).

Portelinha, F.H.M., Bueno, B.S., Zornberg, J.G., 2013. Performance of nonwoven geotextile-reinforced walls under wetting conditions: laboratory and field investigations. Geosynt. Int. 20 (2), 90–104. https://doi.org/10.1680/gein.13.00004.

Prasad, P.S., Ramana, G.V., 2016. Feasibility study of copper slag as a structural fill in reinforced soil structures. Geotext. Geomemb. 44 (4), 623–640. https://doi.org/10.1016/j.geotexmem.2016.03.007.

Razzazan, S., Keshavarz, A., Mosallanezhad, M., 2018. Pullout behavior of polymeric strip in compacted dry granular soil under cyclic tensile load conditions. J. Rock Mech. Geotech. Eng. 10 (5), 968–976. https://doi.org/10.1016/j.jrmge.2018.04.007.

Razzazan, S., Keshavarz, A., Mosallanezhad, M., 2019. Large-scale pullout testing and numerical evaluation of U-shape polymeric straps. Geosynth. Int. 26 (3), 237–250. https://doi.org/10.1680/jgein.19.00001.

Rezende, L.R. de, Camapum-de-Carvalho, J., Palmeira, E.M., 2005. The use of alternative and improved construction materials and geosynthetics for pavements. In: Indraratna, B., Chu, J. (Eds.), Ground Improvement – Case Histories, vol. 3, pp. 447–489. https://doi.org/10.1016/S1571-9960(05)80029-1, 1.

Santos, E.C.G., Palmeira, E.M., Bathurst, R.J., 2014. Performance of two geosynthetic reinforced walls with recycled construction waste backfill and constructed on collapsible ground. Geosynt. Int. 21 (4), 256–269. https://doi.org/10.1680/gein.14.00013.

Schanz, T., Vermeer, P.A., 1996. Angles of friction and dilatancy of sand. Géotechnique 46 (1), 145–151. https://doi.org/10.1680/geot.1996.46.1.145.

Schlosser, F., Bastick, M., 1991. Reinforced earth. In: Fang, H.Y. (Ed.), Foundation Engineering Handbook. Springer, New York, pp. 778–795. https://doi.org/10.1007/978-1-4757-5271-7_21.

Sieira, A.C.C.F., Gerscovich, D.M.S., Sayão, A.S.F.J., 2009. Displacement and load transfer mechanisms of geogrids under pullout condition. Geotext. Geomemb. 27 (4), 241–253. https://doi.org/10.1016/j.geotexmem.2008.11.012.

Simoni, A., Houlsby, G.T., 2006. The direct shear strength and dilatancy of sand-gravel mixtures. Geotech. Geolog. Eng. 24 (3), 523–549. https://doi.org/10.1007/s10706-004-5832-6.

Sukmak, K., Sukmak, P., Horpibulsuk, S., Han, J., Shen, S.-L., Arulrajah, A., 2015. Effect of fine content on the pullout resistance mechanism of bearing reinforcement embedded in cohesive-frictional soils. Geotext. Geomemb. 43 (2), 107–117. https://doi.org/10.1016/j.geotexmem.2014.11.010.

Suksiripattanapong, C., Horpibulsuk, S., Chinkulkijniwat, A., Chai, J.C., 2013. Pullout resistance of bearing reinforcement embedded in coarse-grained soils. Geotext. Geomemb. 36 (1), 44–54. https://doi.org/10.1016/j.geotexmem.2012.10.008.

Tang, C.-S., Li, J., Wang, D.-Y., Shi, B., 2016. Investigation on the interfacial mechanical behavior of wave-shaped fiber reinforced soil by pullout test. Geotext. Geomemb. 44 (6), 872–883. https://doi.org/10.1016/j.geotexmem.2016.05.001.

Teixeira, S.H.C., Bueno, B.S., Zornberg, J.G., 2007. Pullout resistance of individual longitudinal and transverse geogrid ribs. J. Geotech. Geoenv. Eng. 133 (1), 37–50. https://doi.org/10.1061/(ASCE)1090-0241(2007)133:1(37).

Vieira, C.S., Pereira, P.M., Lopes, M. de L., 2016. Recycled construction and demolition wastes as filling material for geosynthetic reinforced structures. Interface properties. J. Cleaner Prod. 124 (1), 299–311. https://doi.org/10.1016/j.jclepro.2016.02.115.

Wang, Z., Jacobs, F., Ziegler, M., 2016. Experimental and DEM investigation of geogrid-soil interaction under pullout loads. Geotext. Geomemb. 44 (3), 230–246. https://doi.org/10.1016/j.geotexmem.2015.11.001.

Yang, Q.-S., Qin, Q.-H., Peng, S.-R., 2003. Size effects in the fiber pullout test. Composite Struct 61 (3), 193–198. https://doi.org/10.1016/S0263-8223(03)00066-7.

Yang, G.-Q., Liu, H., Zhou, Y.-T., Xiong, B.-L., 2014. Post-construction performance of a two-tiered geogrid reinforced soil wall backfilled with soil-rock mixture. Geotext. Geomemb. 42 (2), 91–97. https://doi.org/10.1016/j.geotexmem.2014.01.007.

Zhang, D.-B., Zhang, Y., Cheng, T., 2018. Measurement of grass root reinforcement for copper slag mixed soil using improved shear test apparatus and calculating formulas. Measurement 118 (1), 14–22. https://doi.org/10.1016/j.measurement.2018.01.005.

Zhang, H., Yuan, X., Liu, Y., Wu, J., Song, X., He, F., 2020. Experimental study on the pullout behavior of scrap tire strips and their application as soil reinforcement. Const. Building Mat 254, 1–11. https://doi.org/10.1016/j.conbuildmat.2020.119288.

Zornberg, J.G., Mitchell, J.K., 1994. Reinforced soil structures with poorly draining backfills. Part I: reinforcement interactions and functions. Geosynt. Int. 1 (2), 103–148. https://doi.org/10.1680/gein.1.0006.

Zornberg, J.G., 2002. Discrete framework for limit equilibrium analysis of fibre-reinforced soil. Géotechnique 52 (8), 593–604. https://doi.org/10.1680/geot.2002.52.8.593.